Clim. Past Discuss., 9, 1165–1235, 2013
www.clim-past-discuss.net/9/1165/2013/
doi:10.5194/cpd-9-1165-2013

Climate of the Past
Discussions
Open Access

A reconstruction of radiocarbon production and total solar irradiance from the Holocene ^{14}C and CO_2 records: implications of data and model uncertainties

R. Roth[1,2] and F. Joos[1,2]

[1]Climate and Environmental Physics, Physics Institute, University of Bern, Bern, Switzerland
[2]Oeschger Centre for Climate Change Research, University of Bern, Bern, Switzerland

Received: 7 February 2013 – Accepted: 16 February 2013 – Published: 1 March 2013

Correspondence to: R. Roth (roth@climate.unibe.ch)

Published by Copernicus Publications on behalf of the European Geosciences Union.

Abstract

Past atmospheric CO_2 concentrations reconstructed from polar ice cores combined with its $\Delta^{14}C$ signature as conserved in tree-rings provide important information both on the cycling of carbon as well as the production of radiocarbon (Q) in the atmosphere. The latter is modulated by changes in the strength of the magnetic field enclosed in the solar wind and is a proxy for past changes in solar activity.

We perform transient carbon-cycle simulations spanning the past 21 kyr using Bern3D-LPX, a fully featured Earth System Model of Intermediate Complexity (EMIC) with a 3-D ocean, sediment and a dynamic vegetation model. Using the latest atmospheric IntCal09/SHCal04 radiocarbon records, we reconstruct the Holocene radiocarbon fluxes and the total production rate. Our carbon-cycle based modern estimate of $Q \approx 1.7\,\text{atoms}\,\text{cm}^{-2}\,\text{s}^{-1}$ is lower than previously reported by Masarik and Beer (2009) and more in line with Kovaltsov et al. (2012).

Q is then translated into the solar modulation potential (Φ) using the latest geomagnetic field reconstruction and linked to a recent reanalysis of early instrumental data. In contrast to earlier reconstructions, our record suggests that periods of high solar activity (> 600 MeV) were quite common not only in recent millennia but throughout the Holocene. Solar activity in our decadally-smoothed record is during 28 % of the time higher than the modern average of 650 MeV during the past 9 ka. But due to considerable uncertainties in the normalization of Φ to instrumental data, the absolute value of Φ remains weakly constrained.

Further, our simulations with a spatially resolved model (taking the interhemispheric $\Delta^{14}C$ gradient into account) show that reconstructions that rely on the Northern Hemisphere ^{14}C record only are biased towards low values during the Holocene. Notable deviations on decadal-to-centennial time scales are also found in comparison with earlier reconstructions.

In a last step, past total solar irradiance (TSI) is quantified using a recently published Φ-TSI relationship yielding small changes in Holocene TSI of order $1\,\text{W}\,\text{m}^{-2}$

with a Maunder Minimum irradiance reduction of $0.85 \pm 0.17\,\mathrm{W\,m^{-2}}$. Future extension of TSI using autoregressive modeling suggest a declining solar activity in the next decades towards average Holocene conditions. Past TSI changes are finally translated into changes in surfaces atmospheric temperature (SAT) by forcing the Bern3D-LPX model with our new TSI record, yielding SAT anomalies of less than 0.1 K.

1 Introduction

Solar insolation is the driver of the climate system of the Earth (e.g. Gray et al., 2010; Lockwood, 2012). Variations in total solar irradiance (TSI) have the potential to significantly modify the energy balance of the Earth (Crowley, 2000; Ammann et al., 2007; Jungclaus et al., 2010). However, the magnitude of variations in TSI (Schmidt et al., 2011, 2012; Shapiro et al., 2011; Lockwood, 2012) and its temporal evolution (Solanki et al., 2004; Muscheler et al., 2005b; Schmidt et al., 2011) remain uncertain and are debated. Solar activity and TSI were reconstructed from the Holocene radiocarbon record. These reconstructions relied on box models of the ocean and land carbon cycle or on a 2-dimensional representation of the ocean (Solanki et al., 2004; Marchal, 2005; Usoskin and Kromer, 2005; Vieira et al., 2011; Steinhilber et al., 2012). A quantitative assessment how the climate-carbon cycle changes over the last glacial termination, Holocene and last millennium climate variations, ocean sediment and dynamic vegetation and soil changes affect atmospheric ^{14}C and inferred Holocene ^{14}C production and solar activity is yet missing.

The goal of this study is to reconstruct Holocene radiocarbon production, solar modulation potential to characterize the open solar magnetic field, TSI, and the influence of TSI changes on Holocene climate from the proxy records of atmospheric $\Delta^{14}C$ (McCormac et al., 2004; Reimer et al., 2009) and CO_2 and a recent reconstruction of the geomagnetic field (Korte et al., 2011). The TSI reconstruction is extended into the future to yr 2500 based on its spectral properties. We apply the Bern3D-LPX Earth System Model of Intermediate Complexity that features a 3-dimensional dynamic ocean,

CPD
9, 1165–1235, 2013

reactive ocean sediments, a Dynamic Global Vegetation Model (DGVM), an energy-moisture balance atmosphere, and cycling of carbon and carbon isotopes. The model is forced by changes in orbital parameters, explosive volcanic eruptions, well mixed greenhouse gases (CO_2, CH_4, N_2O), aerosols, ice cover and land use area changes. Bounding scenarios for deglacial radiocarbon changes and Monte Carlo techniques are applied to comprehensively quantify uncertainties.

TSI reconstructions that extend beyond the satellite record must rely on proxy information. ^{14}C and ^{10}Be are two proxies that are particularly well suited (Beer et al., 1983; Muscheler et al., 2008; Steinhilber et al., 2012); their production by cosmic particles is directly modulated by the strength of the solar magnetic field and they are conserved in ice cores (^{10}Be) and tree rings (^{14}C). The redistributions of ^{10}Be and ^{14}C within the climate system follow very different pathways and thus the two isotopes can provide independent information. The ^{10}Be and ^{14}C proxy records yield in general consistent reconstructions of isotope production and solar activity with correlations exceeding 0.8 (Bard et al., 1997; Lockwood and Owens, 2011). Important caveats, however, and differences in detail remain. After production, ^{10}Be is attached to aerosols and variations in atmospheric transport and dry and wet deposition of ^{10}Be and incorporation into the ice archive lead to noise and uncertainties. This is highlighted by the opposite, and not yet understood, 20th century trends in ^{10}Be in Greenland versus Antarctic ice cores (Muscheler et al., 2007; Steinhilber et al., 2012). Thus, taken at face value, Greenland and Antarctic ^{10}Be records suggest opposite trends in solar activity in the 20th century. ^{14}C is oxidized after production and becomes as $^{14}CO_2$ part of the global carbon cycle. It enters the ocean-sediment and the land biosphere and is removed from the climate system by radioactive decay with an average life time of 8267 yr. Atmospheric ^{14}C is influenced not only by short-term production variations, but also by variations of the coupled carbon cycle-climate system, and their evolutions due to the long-timescales governing radioactive decay and carbon overturning in the land and ocean.

The conversion of the radiocarbon proxy record (McCormac et al., 2004; Reimer et al., 2009) to TSI involves several steps. First a carbon cycle model is applied to infer

CPD
9, 1165–1235, 2013

radiocarbon production by deconvolving the atmospheric radiocarbon budget. Radiocarbon production is equal to the prescribed changes in the atmospheric radiocarbon inventory and decay in the atmosphere plus the modeled net air-to-sea and net air-to-land ^{14}C fluxes. The radiocarbon signature of a flux or a reservoir is commonly reported in the $\Delta^{14}C$-notation, i.e. as the fractionation-corrected per mil deviation of $^{14}R = {}^{14}C/{}^{12}C$ from a given standard defined as $^{14}R_{std} = 1.176 \times 10^{-12}$ (Stuiver and Polach, 1977). ^{14}C production depends on the magnitude of the shielding of the Earth's atmosphere by the geomagnetic and the open solar magnetic field. Reconstructions of the geomagnetic field can thus be combined with a mechanistic cosmogenic isotope production model (Masarik and Beer, 1999, 2009; Kovaltsov et al., 2012) to infer the strength of the solar magnetic field as expressed by the so called solar modulation potential, Φ. Finally, Φ is translated into variations in TSI.

Each of these steps has distinct uncertainties and challenges. Deglacial carbon cycle changes are large and atmospheric CO_2 increased from 180 ppm at the Last Glacial Maximum to 265 ppm 11 kyr BP. These variations are thought to be driven by physical and biogeochemical reorganizations of the ocean (e.g. Brovkin et al., 2012; Menviel et al., 2012). They may influence the ^{14}C evolution in the Holocene and the deconvolution for the ^{14}C production, but were not considered in previous studies. Many earlier studies (Marchal, 2005; Muscheler et al., 2005a; Usoskin and Kromer, 2005; Vonmoos et al., 2006; Steinhilber et al., 2012) deconvolving the ^{14}C record relied on simplified box models using a perturbation approach (Oeschger et al., 1975; Siegenthaler, 1983) where the natural marine carbon cycle is not simulated and climate and ocean circulation and land carbon turnover is kept constant. In the perturbation approach, the ocean carbon and radiocarbon inventory is underestimated by design as the concentration of dissolved inorganic carbon is set to its surface concentration. ^{12}C and ^{14}C are not transported as separate tracer but combined into a single tracer, the $^{14}C/^{12}C$ ratio. These shortcomings, however, can be overcome by applying a spatially-resolved coupled carbon cycle-climate model that includes the natural carbon cycle and its anthropogenic perturbation and where ^{12}C and ^{14}C are distinguished.

CPD
9, 1165–1235, 2013

A key target data set is the data of the Global Ocean Data Analysis Project (GLODAP) that include station data and gridded data of dissolved inorganic carbon and its ^{14}C signature (Key et al., 2004). This permits one the quantification of the oceanic radiocarbon inventory, the by far largest radiocarbon inventory on earth. Together with data-based estimates of the carbon inventory on land, atmosphere, and reactive sediment and their signatures the global radiocarbon inventory and thus the long-term, average ^{14}C production can be reliably estimated. Further, the spatial carbon and ^{14}C distribution within the oceans is a yard stick to gauge the performance of any ocean circulation and carbon cycle model. ^{14}C permit the quantification of the overturning timescales within the ocean (e.g. Müller et al., 2006) and of the magnitude of the air-sea carbon exchange rate (e.g. Naegler and Levin, 2006; Sweeney et al., 2007; Müller et al., 2008).

The conversion of the radiocarbon production record into Φ requires knowledge on the strength of the geomagnetic field that together with the open solar magnetic field contributes to the shielding of the Earth's atmosphere from the cosmic ray flux. Recently, updated reconstructions of the earth magnetic field have become available (Knudsen et al., 2008; Korte et al., 2011). The paleoproxy record of Φ should be consistent with instrumental observations. The deconvolution of the atmospheric ^{14}C history for natural production variations is only possible up to about 1950 AD. Afterward, the atmospheric ^{14}C content almost doubled due to atomic bomb tests in the fifties and early sixties of the 20th century and uncertainties in this artificial ^{14}C production are larger than natural production variations. This limits the overlap of the ^{14}C-derived paleoproxy record of Φ with reconstructions of Φ based on balloon-borne measurements and adds uncertainty to the normalization of the paleo proxy record to recent data. How variations in cosmogenic isotope production and in Φ are related to TSI is unclear and there is a lack of mechanistic understanding. This is also reflected in the large spread in past and recent reconstructions of TSI variability on multi-decadal to centennial timescales (e.g. Bard et al., 2000; Lean, 2000; Wang et al., 2005; Steinhilber et al., 2009; Steinhilber et al., 2012; Shapiro et al., 2011; Schrijver et al., 2011). Recent

CPD
9, 1165–1235, 2013

reconstructions based on the decadal-scale trend found in the TSI satellite record reveal small amplitude variations in TSI of order $1\,\mathrm{W\,m^{-2}}$ over past millennia (Steinhilber et al., 2009), whereas others based on observations of the most quiet area on the present Sun, suggest that TSI variations are of order $6\,\mathrm{W\,m^{-2}}$ or even more (Shapiro et al., 2011).

The outline of this study is as follows. Next, we will describe the carbon cycle model and methods applied. In the results Sect. 3, we first characterize the model response by applying a large set of sinusoidal perturbations in atmospheric ^{14}C. In Sect. 3.2, we discuss the radiocarbon and carbon inventory and distribution in the model in comparison with observations (Sect. 3.1), before turning to the time evolution of the carbon fluxes, the atmospheric carbon budget, and of radiocarbon production in Sect. 3.2. In Sects. 3.3 to 3.5 results are presented for the solar activity, TSI, and simulated, solar-driven changes in global mean surface air temperature over the Holocene and extrapolated TSI variations up to year 2500. Discussion and conclusions follow in Sect. 4 and the appendix present error calculations for ^{14}C production, solar modulation, and TSI in greater detail.

2 Methodology

2.1 Carbon-cycle model description

The Bern3D-LPX climate-carbon cycle model is an Earth System Model of Intermediate Complexity and includes an energy and moisture balance atmosphere and sea ice model (Ritz et al., 2011), a 3-dimensional dynamic ocean (Müller et al., 2006), a marine biogeochemical cycle (Tschumi et al., 2008; Parekh et al., 2008), an ocean sediment (Tschumi et al., 2011), and a dynamic global vegetation model (Sitch et al., 2003) (Fig. 1). Total carbon and the stable isotope ^{13}C and the radioactive isotope ^{14}C are transported individually as tracers in the atmosphere-ocean-sediment-land biosphere system.

CPD
9, 1165–1235, 2013

The geostrophic-frictional balance 3-D ocean component is based on Edwards and Marsh (2005) and as further improved by Müller et al. (2006). It includes an isopycnal diffusion scheme and Gent-McWilliams parametrization for eddy-induced transport (Griffies, 1998). Here, a horizontal resolution of 36 × 36 grid boxes and 32 layers in the vertical is used. Wind stress is prescribed according to the monthly climatology from NCEP/NCAR (Kalnay et al., 1996). Thus, changes in ocean circulation in response to changes in wind stress under varying climate are not simulated.

The atmosphere is represented by a 2-D energy and moisture balance model with the same horizontal resolution as the ocean (Ritz et al., 2011). Following Weaver et al. (2001), outgoing longwave radiative fluxes are parametrized after Thompson and Warren (1982) with additional radiative forcings due to CO_2, other greenhouse gases, volcanic aerosols, and a feedback parameter, chosen to produce an equilibrium climate sensitivity of 3 °C for a nominal doubling of CO_2. The past extent of Northern Hemisphere ice sheets is prescribed following the ICE4G model (Peltier, 1994) as described in Ritz et al. (2011).

The marine biogeochemical cycling of carbon, alkalinity, phosphate, oxygen, silica, and of the carbon isotopes is detailed by Parekh et al. (2008) and Tschumi et al. (2011). Remineralisation of organic matter in the water column as well as air-sea gas exchange is implemented according to the OCMIP-2 protocol (Orr and Najjar, 1999; Najjar et al., 1999). However, the piston velocity now scales linear (instead of a quadratic dependence) with wind speed following Krakauer et al. (2006). The global mean air-sea transfer rate is reduced by 17 % compared to OCMIP-2 to match observation-based estimates of natural and bomb-produced radiocarbon (Müller et al., 2008) and in agreement with other studies (Sweeney et al., 2007; Krakauer et al., 2006; Naegler and Levin, 2006). Prognostic formulations link marine productivity and export production of particulate and dissolved organic matter (POM, DOM) to available nutrients (P, Fe, Si), temperature, and light in the euphotic zone. Carbon is represented as tracers DIC, (dissolved inorganic carbon), DIC-13, DIC-14 and labile DOC (dissolved organic

CPD
9, 1165–1235, 2013

carbon), DOC-13, and DOC-14. Particulate matter (POM and $CaCO_3$) is remineralized/dissolved in the water column applying a Martin-type power-law curve.

A 10-layer sediment diagenesis model (Heinze et al., 1999; Gehlen et al., 2006) is coupled to the ocean floor dynamically calculating the advection, remineralization/redissolution and bioturbation of solid material in the top 10 cm ($CaCO_3$, POM, opal and clay) as well as pore-water chemistry and diffusion as described in detail in Tschumi et al. (2011). In contrast to the setup in Tschumi et al. (2011), the initial alkalinity inventory in the ocean is increased from 2350 to 2460 $\mu mol\,kg^{-1}$ in order to get a realistic present-day DIC inventory (Key et al., 2004).

The land biosphere model is based on the Lund-Potsdam-Jena (LPJ) Dynamic Global Vegetation Model (DGVM) with a resolution of $3.75 \times 2.5^{\circ}$ as used in Joos et al. (2001), Gerber et al. (2003), Joos et al. (2004) and described in detail in Sitch et al. (2003). The fertilization of plants by CO_2 is calculated according to the modified Farquhar scheme (Farquhar et al., 1980). A landuse conversion module has been added to take into account anthropogenic land cover change (ALCC) (Strassmann et al., 2008; Stocker et al., 2011). Isotopic discrimination of ^{13}C during stomatal transport and photosynthesis by C3 and C4 plants is as implemented by Scholze et al. (2003).

2.2 Experiment protocol

The model is initialized as follows: (i) the ocean-atmosphere system is brought into preindustrial (PI) steady-state (Ritz et al., 2011). (ii) The ocean's biogeochemical (BGC) and sediment component is spun up over 50 kyr. During this spin-up phase, the loss of tracers due to solid material seafloor burial is compensated by spatially uniform weathering fluxes to the surface ocean. These weathering input fluxes are diagnosed at the end of the sediment spin-up and kept constant thereafter. (iii) The coupled model is forced into a last glacial maximum (LGM)-state by applying corresponding orbital settings, GHG's radiative forcing, freshwater-relocation from the ocean to the ice-sheets and a LGM dust influx field. Atmospheric trace gases CO_2 (185 ppm), $\delta^{13}C$ (−6.4 ‰) and $\Delta^{14}C$ (432 ‰) are prescribed. The model is then allowed to re-equilibrate for 50 kyr.

CPD
9, 1165–1235, 2013

Next, the model is integrated forward in time from 21 kyr BP until yr 1950 AD using the following natural and anthropogenic external forcings (Figs. 2, 3 and 4): atmospheric CO_2 as compiled by Joos and Spahni (2008), $^{13}CO_2$ (Francey et al., 1999; Elsig et al., 2009; Schmitt et al., 2012), $\Delta^{14}C$ of CO_2 (McCormac et al., 2004; Reimer et al., 2009), orbital parameters (Berger, 1978), radiative forcing due to GHG's CO_2, CH_4 and N_2O (Joos and Spahni, 2008). Iron-fertilization is taken into account by interpolating LGM (Mahowald et al., 2006) and modern dust forcing (Luo et al., 2003) following a spline-fit to the EDC dust record (Lambert et al., 2008). Shallow water carbonate deposition history is taken from Vecsei and Berger (2004). The ice sheet extent (including fresh-water relocation and albedo changes) during the deglaciation is scaled between LGM and modern fields of Peltier (1994) using the benthic $\delta^{18}O$ stack of Lisiecki and Raymo (2005) which was lowpass-filtered with a cutoff period of 10 kyr. From 850–1950 AD volcanic aerosols (based on Crowley, 2000, prepared by UVic), sulphate aerosol forcing applying the method by Reader and Boer (1998) detailed by Steinacher (2011), total solar irradiance forcing from PMIP3/CMIP5 (Wang et al., 2005; Delaygue and Bard, 2011) and carbon emissions from fossil fuel and cement production are taken into account (Andres et al., 1999).

The land module is forced by a 31-yr monthly CRU climatology for temperature, precipitation and cloud cover. On this CRU-baseline climatology, we superpose interpolated anomalies from snapshot-simulations performed with the HadCM3 model (Singarayer and Valdes, 2010). In addition, global mean temperature deviation w.r.t. 850 AD are used to scale climate anomaly fields obtained from global warming simulations with the NCAR AOGCM from 850–1950 AD applying a linear pattern scaling approach (Joos et al., 2001). Changes in sea-level and ice sheet extent influence the number and locations of grid cells available for plant growth and carbon storage; we apply interpolated landmasks from the ICE5G-VM2 model (Peltier, 2004). Anthropogenic land cover change during the Holocene is prescribed following the HYDE 3.1 dataset (Klein Goldewijk, 2001; Klein Goldewijk and van Drecht, 2006).

CPD
9, 1165–1235, 2013

R. Roth and F. Joos

In all transient simulations, the model's atmosphere is forced with the IntCal09 (21 kyr BP to 1950 AD, Reimer et al., 2009) and SHCal04 (11 kyr BP to 1950 AD, McCormac et al., 2004) for the Northern and Southern Hemisphere, respectively (Fig. 2a). For the equatorial region (20° N to 20° S), we use the arithmetic mean of these two records. Since SHCal04 does not reach as far back in time as the IntCal09 record, we use IntCal09 data for both hemispheres before 11 kyr BP. Between the 5-yr spaced data points given by these records, cubic interpolation is applied.

The Earth System underwent a major reorganization during the last glacial termination as evidenced by warming, ice sheet retreat, sea level rise and an increase in CO_2 and other GHGs (Shackleton, 2001; Clark et al., 2012). Memory effects associated with the long life time of radiocarbon (8267 yr) and the long time scales involved in ocean-sediment interactions imply that processes during the last glacial termination (ca. 18 to 11 kyr BP) influence the evolution of carbon and radiocarbon during the Holocene (Menviel and Joos, 2012). Although many hypotheses are discussed in the literature on the mechanism governing the deglacial CO_2 rise (e.g. Köhler et al., 2005; Brovkin et al., 2007; Tagliabue et al., 2009; Bouttes et al., 2011; Menviel et al., 2012), it remains unclear how individual processes have quantitatively contributed to the reconstructed changes in CO_2 and $^{14}CO_2$ over the termination. The identified processes may be distinguished into three classes: (i) relatively-well known mechanisms such as changes in temperature, salinity, an expansion of North Atlantic Deep Water, sea ice retreat, a reduction in iron input and carbon accumulation on land as also represented in our standard model setup, (ii) an increase in deep ocean ventilation over the termination as suggested by a range of proxy data (e.g. Franois et al., 1997; Adkins et al., 2002; Hodell et al., 2003; Galbraith et al., 2007; Anderson et al., 2009; Schmitt et al., 2012; Burke and Robinson, 2012) and modeling work (e.g. Tschumi et al., 2011) (iii) a range of mechanisms associated with changes in the marine biological cycling of organic carbon, calcium carbonate, and opal in addition to those included in (i).

The relatively well-known forcings implemented in our standard setup explain only about half of the reconstructed CO_2 increase over the termination (Menviel et al., 2012).

CPD
9, 1165–1235, 2013

This indicates that the model misses important processes or feedbacks concerning the cycling of carbon. To this end, we apply two idealized scenarios for this missing mechanism, regarded as bounding cases in terms of their impacts on atmospheric $\Delta^{14}C$. In the first scenario, termed CIRC, the atmospheric carbon budget over the termination is approximately closed by forcing changes in deep ocean ventilation. In the second, termed BIO, the carbon budget is closed by imposing changes in the biological cycling of carbon.

^{14}C in the atmosphere and the deep ocean is sensitive to the surface-to-deep transport of ^{14}C. This ^{14}C transport is dominated by physical transport (advection, diffusion, convection), whereas biological fluxes play a small role. Consequently, processes reducing the thermohaline circulation (THC), the surface-to-deep transport rate, and deep ocean ventilation tend to increase $\Delta^{14}C$ of atmospheric CO_2 and to decrease $\Delta^{14}C$ of DIC in the deep. Recently, a range of observational studies addressed deglacial changes in radiocarbon and deep ocean ventilation. Some authors report extremely high ventilation ages up to 5000 yr (Marchitto et al., 2007; Bryan et al., 2010; Skinner et al., 2010; Thornalley et al., 2011) while others find no evidence for such an old abyssal water mass (De Pol-Holz et al., 2010). In contrast, changes in processes related to the biologic cycle of carbon such as changes in export production or the remineralization of organic carbon hardly affect $\Delta^{14}C$ of DIC and CO_2 despite their potentially strong impact on atmospheric CO_2 (e.g. Tschumi et al., 2011).

Technically, these two bounding cases are realized as follow. In the experiment BIO, we imply (in addition to all other forcings) a change in the depth where exported particulate organic matter is remineralized; the exponent (α) in the power-law describing the vertical POM flux profile (Martin curve) is increased during the termination from a low glacial value (Fig. 3f). A decrease in the average remineralisation depth over the termination leads to an increase in atmospheric CO_2 (Matsumoto, 2007; Kwon et al., 2009; Menviel et al., 2012), but does not substantially affect $\Delta^{14}C$. α is increased from 0.8 to 1.0 during the termination in BIO, while in the other experiments α is set to 0.9. In experiment, CIRC, ocean circulation is strongly reduced at the LGM by reducing the windstress globally by 50 % relative to modern values. The windstress is then linearly relaxed to modern values over the termination (18 to 11 kyr BP, Fig. 3f). This leads to a transfer of old carbon from the deep ocean to the atmosphere, rising atmospheric CO_2 and lowering $\Delta^{14}C$ of CO_2 (Tschumi et al., 2011). We stress that changes in wind stress and remineralisation depth are used here as tuning knobs and not considered as realistic.

To further assess the sensitivity of the diagnosed radiocarbon production on the cycling of carbon and climate, we perform a simulation (CTL) where all forcings except atmospheric CO_2 (and isotopes) are kept constant at PI values. This setup corresponds to earlier box-model studies where the Holocene climate was assumed to be constant.

2.3 The production rate of radiocarbon, Q

The ^{14}C production rate Q is diagnosed by solving the atmospheric ^{14}C budget equation in the model. The model calculates the net fluxes from the atmosphere to the land biosphere ($^{14}F_{ab}$) and to the ocean ($^{14}F_{as}$) under prescribed $^{14}CO_2$ for a given carbon-cycle/climate state. Equivalently, the changes in ^{14}C inventory and ^{14}C decay of individual land and ocean carbon reservoirs are computed. Data-based estimates for the ocean and land inventory are used to match preindustrial radiocarbon inventories as close as possible. The production rate is then given at any time t by:

$$
\begin{aligned}
Q(t) = {} & \frac{I_{\text{atm,data}}(t)}{\tau} + \frac{dI_{\text{atm,data}}(t)}{dt} + {}^{14}F_{\text{budget}}(t) \\
& \left.\begin{aligned}
&+ \frac{I_{\text{ocn,model}}(t)}{\tau} + \frac{dI_{\text{ocn,model}}(t)}{dt} + \frac{\Delta I_{\text{ocn,data-model}}(t=t_0)}{\tau} \\
&+ \frac{I_{\text{sed,model}}(t)}{\tau} + \frac{dI_{\text{sed,model}}(t)}{dt} + {}^{14}F_{\text{burial}}(t)
\end{aligned}\right\} = {}^{14}F_{\text{as}} \\
& + \frac{I_{\text{lnd,model}}(t)}{\tau} + \frac{dI_{\text{lnd,model}}(t)}{dt} + \frac{\Delta I_{\text{lnd,data-model}}(t=t_0)}{\tau} \quad = {}^{14}F_{\text{ab}}.
\end{aligned}
\tag{1}
$$

Here, I and F denote ^{14}C inventories and fluxes, τ (8267 yr) is the mean ^{14}C lifetime with respect to radioactive decay. Subscripts atm, ocn, sed, and lnd refer to the atmosphere, the ocean, reactive ocean sediments, and the land biosphere. Subscript data

CPD
9, 1165–1235, 2013

indicate that terms are prescribed from reconstructions and subscript model that values are calculated with the model. ${}^{14}F_{\text{burial}}$ is the net loss of ^{14}C associated with the weathering-burial carbon fluxes. $\Delta I_{\text{ocn,data-model}}(t=t_0)$ represents a (constant) correction, defined as the difference between the modelled and observation-based inventory of DI^{14}C in the ocean plus an estimate of the ^{14}C inventory associated with refractory DOM not represented in our model. In analogue, $\Delta I_{\text{lnd,data-model}}(t=t_0)$ denotes a constant ^{14}C decay rate associated with terrestrial carbon pools not simulated in out model. ${}^{14}F_{\text{budget}}$ is a correction associated with the carbon flux diagnosed to close remaining imbalances in the atmospheric CO_2 budget.

Observation-based versus simulated ocean radiocarbon inventory: The global ocean inorganic radiocarbon inventory is estimated using the gridded data provided by GLODAP for the preindustrial state (Key et al., 2004) and in-situ density calculated from World Ocean Atlas 2009 (WOA09) temperature and salinity fields (Antonov et al., 2010; Locarnini et al., 2010). Since not the entire ocean is covered by the GLODAP data, we fill these gaps by assuming global mean ^{14}C concentration in these regions (e.g. in the Arctic ocean). The result of this exercise is 3.27×10^6 mol of DI^{14}C. Hansell et al. (2009) estimated a global refractory DOC inventory of 624 GtC. Δ^{14}C of DOC measurements are rare, but data in the central North Pacific (Bauer et al., 1992) suggest high radiocarbon ages of ∼6000 yr, corresponding to a Δ^{14}C value of −526 ‰. Taking this values as representative yields additional 2.9×10^4 mol ^{14}C. The preindustrial ^{14}C inventory associated with labile DOM is estimated from our model results to be 1.3×10^3 mol ^{14}C. This yields a data-based radiocarbon inventory associated with DIC and labile and refractory DOM in the ocean of 3.30×10^6 mol. The corresponding preindustrial modelled ocean inventory yields 3.05×10^6 mol for BIO, 3.32×10^6 mol for CIRC and 3.10×10^6 mol for CTL. Thus, the correction $\Delta I_{\text{ocn,data-model}}(t=t_0)$ is less than 8 % in the case of BIO and less than 1 % for CIRC and CTL.

Observation-based versus simulated terrestrial radiocarbon inventory: As our model for the terrestrial biosphere does not include carbon stored as peatlands and permafrost soils. We estimate this pool to contain approximately 1000 GtC of old carbon with a isotopic signature of −400‰ (thus roughly one half-life old). Although small compared to the uncertainty in the oceanic inventory, we include these 5.9×10^4 mol of ^{14}C in our budget as a constant correction $\Delta I_{\text{lnd,data-model}}(t = t_0)$.

Closing the atmospheric CO_2 *budget:* The atmospheric carbon budget is closed in the transient simulations by diagnosing an additional carbon flux F_{budget}:

$$F_{\text{budget}} = -\frac{dN_{\text{atm,data}}}{dt} - E + F_{\text{as}} + F_{\text{ab}} \tag{2}$$

where the change in the atmospheric carbon inventory (dN_{atm}/dt) is prescribed from ice core data, E are fossil fuel carbon emissions, and F_{as} and F_{ab} the net carbon fluxes into the ocean and the land biosphere. The magnitude of this inferred emission indicates the discrepancy between modelled and ice core CO_2 and provides a measure how well the model is able to simulate the reconstructed CO_2 evolution. We assign to this flux (of unknown origin) a $\Delta^{14}C$ equal the contemporary atmosphere and an associated uncertainty in $\Delta^{14}C$ of ±200 ‰. This is not critical as F_{budget} and associated uncertainties in the ^{14}C budget are generally small over the Holocene for simulations CIRC and BIO (see appendix Fig. A1e).

The production rate is either reported as mol yr^{-1} or alternatively $\text{atoms cm}^{-2}\,\text{s}^{-1}$. The atmospheric area and scaleheight are set to $5.10 \times 10^{14}\,\text{m}^2$ and 8194 m in our model, therefore the two quantities are related as $1\,\text{atom cm}^{-2}\,\text{s}^{-1} = 267.0\,\text{mol yr}^{-1}$.

2.4 Solar activity

Radiocarbon, as other cosmogenic radionuclides are produced in Earth's upper atmosphere due to nuclear reactions induced by high-energy galactic cosmic rays (GCR). Far away from the solar system, this flux is to a good approximation constant in time, but the intensity reaching the Earth is modulated by two mechanism: (i) the shielding effect of the geomagnetic dipole-field and (ii) the modulation due to the magnetic field enclosed in the solar wind. By knowing the past history of the geomagnetic dipole-moment and the production rate of radionuclide, the "strength" of solar activity can therefore be calculated.

The Sun's activity is parametrized by a scalar parameter in the force-field approximation, the so-called solar modulation potential Φ (Gleeson and Axford, 1968). This parameter describes the modulation of the local interstellar spectrum (LIS) at 1 AU. A high solar activity (i.e. a high value of Φ) leads to a stronger magnetic shielding of GCR and thus lowers the production rate of cosmogenic radionuclides. Similarly, the production rate decreases with a higher geomagnetic shielding, expressed as the virtual axis dipole moment (VADM).

The calculation of the normalized (relative to modern) Q for a given VADM and Φ is based on particle simulations performed by Masarik and Beer (1999). This is the standard approach to convert cosmogenic radionuclides production rates into solar activity as applied by Muscheler et al. (2007) and Steinhilber et al. (2008); Steinhilber et al. (2012), but differs from the model recently used by Vieira et al. (2011). The GCR flux entering the solar system is assumed to remain constant within this approach, even though Miyake et al. (2012) found recently evidence for a short-term spike in annual Δ^{14}C data with an extra-solar origin (Hambaryan and Neuhäuser, 2013).

At the time of writing, three reconstructions of the past geomagnetic field are available to us spanning the past 10 kyr (Yang et al., 2000; Knudsen et al., 2008; Korte et al., 2011) shown in Fig. 11 together with the VADM value of 8.22×10^{22} Am^{-2} for the period 1840–1990 estimated by Jackson et al. (2000). The reconstructions by Yang et al. (2000) and Knudsen et al. (2008) relying both on the same database (GEOMAGIA 50) were extensively used in the past for solar activity reconstructions (Muscheler et al., 2007; Steinhilber et al., 2008; Steinhilber et al., 2012; Vieira et al., 2011). We use the most recently published reconstruction by Korte et al. (2011) for our calculations.

For conversion from Φ into TSI, we follow the procedure outlined in Steinhilber et al. (2009, 2010) which consists of two individual steps. First, the radial component of the interplanetary magnetic field, B_r, is expressed as a function of Φ:

CPD
9, 1165–1235, 2013

$$|B_r(t)| = 0.56\,B_{\mathrm{IMF},0} \times \left(\frac{\phi(t)\,v_{\mathrm{SW},0}}{\phi_0\,v_{\mathrm{SW}}}\right)^{1/\alpha} \times \left[1 + \left(\frac{R_{\mathrm{SE}}\,\varpi\cos\Psi}{v_{\mathrm{SW}}(t)}\right)^2\right]^{-\frac{1}{2}}, \tag{3}$$

where v_{SW} is the solar wind speed, $B_{\mathrm{IMF},0}$, ϕ_0, $v_{\mathrm{SW},0}$ are normalization factors, R_{SE} is the mean Sun–Earth distance, ϖ the angular solar rotation rate and Ψ the heliographic latitude. The factor 0.56 has been introduced to adjust the field obtained from the Parker theory with observations. The exponent is set to be in the range $\alpha = 1.7 \pm 0.3$ as in Steinhilber et al. (2009).

Second, the B_r-TSI relationship derived by Fröhlich (2009) is used to calculate the total solar irradiance:

$$\mathrm{TSI} = (1364.64 \pm 0.40)\,\mathrm{W\,m^{-2}} + (0.38 \pm 0.17)\,\mathrm{W\,m^{-2}\,nT^{-1}}\,B_r. \tag{4}$$

This model of converting B_r into TSI is not physically based, but results from a fit to observations for the relatively short epoch where high-quality observational data is available. Note that the B_r-TSI relationship is only valid for solar cycle minima, therefore an artificial sinusoidal solar cycle has to be added to the (solar cycle averaged) Φ before applying Eqs. (3) and (4). In the results section, we show for simplicity solar cycle averages (i.e. without the artificial 11 yr solar cycle).

A point to stress is that the amplitude of low frequency TSI variations is limited by Eq. 4 and small. This is a consequence of the assumption underlying Eq. (4) that recent satellite data, which show a limited decadal-scale variability in TSI, can be extrapolated to past centuries and millennia. Small long-term variations in TSI are in agreement with a range of recent reconstructions (Schmidt et al., 2011) (Climate forcing reconstructions for use in the PMIP simulations of the last millennium), but in conflict with Shapiro et al. (2011) who report much larger TSI variations.

CPD
9, 1165–1235, 2013

Title Page
Abstract | Introduction
Conclusions | References
Tables | Figures
◀| |▶
◀ ▶
Back | Close
Full Screen / Esc
Printer-friendly Version
Interactive Discussion

3 Results

3.1 Sensitivity experiments

We start discussion by analyzing the response of the Bern3D-LPX model to regular sinusoidal changes in the atmospheric radiocarbon ratio. The theoretical background is that any time series can be translated into its power spectrum using Fourier transformation. Thus, the response of the model to perturbations with different frequencies characterizes the model for a given state (climate, CO_2, land use area, etc). The experimental setup for this sensitivity simulation is as follows. $\Delta^{14}C$ is varied according to a sine wave with an amplitude of 10‰ and distinct period. The sine wave is repeated until the model response is at equilibrium. Periods between 5 and 1000 yr are selected. Atmospheric CO_2 (278 ppm), climate and all other boundary conditions are kept fixed at preindustrial values. The natural carbon cycle acts like a smoothing filter and changes in atmospheric $\Delta^{14}C$ arising from variations in Q are attenuated and delayed (Fig. 5a). That is the relative variations in $\Delta^{14}C$ are smaller than the relative variations in Q. Here, we are interested to invert this natural process and to diagnose Q from reconstructed variations in radiocarbon. Consequently, we analyze not the attenuation of the radiocarbon signal, but the amplification of Q for a given variation in atmospheric radiocarbon. Figure 5a shows the amplification in Q, defined as the relative change in Q divided by the relative change in the radiocarbon to carbon ratio, ^{14}R. For example, an amplification of 10 means that if ^{14}R oscillates by 1 % then Q oscillates by 10 % around its mean value. The amplification is largest for high-frequency variations and decreases from above 100 for a period of 5 yr to around 10 for a period of 1000 yr and to 2 for a period of 10 000 yr. High-frequency variations in the ^{14}C reconstruction arising from uncertainties in the radiocarbon measurements may thus translate into significant uncertainties in Q. We will address this problem in the following sections by applying smoothing splines (Enting, 1987) to remove high-frequency variations from the CO_2 and $\Delta^{14}C$ records and by applying a Monte Carlo procedure to vary measurements within their uncertainties (see Appendix A1).

CPD
9, 1165–1235, 2013

The atmospheric radiocarbon anomaly induced by variation in production is partly mitigated through radiocarbon uptake by the ocean and the land. The relative importance of land versus ocean uptake of the perturbation depends strongly on the time scale of the perturbation (Fig. 5b). For annual to decadal-scale perturbations, the ocean and the land uptake are roughly of equal importance. This can be understood by considering that the net primary productivity on land (60 GtC per yr) is of similar magnitude as the gross air-to-sea flux of CO_2 (57 GtC per yr) into the ocean. Thus, these fluxes carry approximately the same amount of radiocarbon away from the atmosphere. On the other hand, if the perturbation in production is varying slower than the typical overturning time scales of the ocean and the land biosphere, then the radiocarbon perturbation in the ratio is distributed roughly proportional to the carbon inventory of the different reservoirs (or to the steady-state radiocarbon flux to the ocean and the land, i.e. 430 vs 29.1 mol yr^{-1}). Consequently, the ratio between the ^{14}C-flux anomalies into ocean and land, $\Delta F_{as} : \Delta F_{ab}$ (w.r.t. to a unperturbed state) is higher the slower the frequency of the applied perturbation (Fig. 5b). Note that these results are largely independent of the magnitude in the applied Δ^{14}C variations; we run these experiments with amplitudes of ±10 and ±100 ‰. Assuming a constant carbon-cycle and climate, Q can be calculated by replacing the carbon cycle-climate model by the model-derived Fourier filter (Fig. 5a) (Usoskin and Kromer, 2005).

Preindustrial carbon and radiocarbon inventories

The loss of ^{14}C is driven by the radioactive decay flux in the different reservoir. The base level of this flux is proportional to the ^{14}C inventory and a reasonable representation of these inventories is thus a prerequisite to estimate ^{14}C production rates. In the following, modelled and observation-based carbon and radiocarbon inventories before the onset of industrialisation are compared (Table 1) and briefly discussed.

The atmospheric ^{14}C inventory is given by the CO_2 and Δ^{14}C input data and therefore fully determined by the forcing and their uncertainty. The ocean model represents the observation-based estimate of the global ocean ^{14}C inventory within 1 % for the

CPD
9, 1165–1235, 2013

setup CIRC and within 8 % for the setup BIO. These deviations are within the uncertainty of the observational data. Nevertheless, this offset is corrected for when Q is calculated (see Eq. 1).

The model is also able to represent the observation-based spatial distribution of ^{14}C in the ocean (Fig. 7). Both observations and model results show highest ^{14}C concentrations in the thermocline of the Atlantic ocean and lowest concentrations in the deep North Pacific. Deviations between modeled and reconstructed concentrations are less than 5 % and typically less than 2 % The model shows in general too high radiocarbon concentrations in the upper 1000 m, while the concentration is lower than indicated by the GLODAP data at depth.

Modelled loss of radiocarbon by sedimentary processes, namely burial of POM and $CaCO_3$ into the diagenetically consolidated zone and particle and dissolution fluxes from/to the ocean, accounts for 52 $mol\,yr^{-1}$ (or roughly 11 % of the total ^{14}C sink). This model estimate may be on the high side as the ocean-to-sediment net flux in the Bern3D model of 0.5 $GtC\,yr^{-1}$ is slightly higher than independent estimates in the range of 0.2 to 0.4 $GtC\,yr^{-1}$.

The total simulated carbon stored in living biomass and soils is 1930 GtC. As discussed above, this is order 1000 GtC lower than best estimates, mainly because peat and permafrost dynamics (Yu et al., 2010; Spahni et al., 2012) are not explicitly simulated in the LPX version applied here. The model-data discrepancy in carbon is less than 3 % of the total carbon inventory in ocean, land, and atmosphere. It translates into 5.9×10^5 mol of ^{14}C when assuming a $\Delta^{14}C$ of −400 ‰ for this old biomass. This is well within the uncertainty range of the total ^{14}C inventory.

3.2 Transient results for the carbon budget and deep ocean ventilation

Next, we discuss how global mean temperature, deep ocean ventilation, and the carbon budget evolved over the past 20 kyrs in our two bounding simulations (CIRC and BIO). Global average surface atmospheric temperature (SAT, Fig. 6a) and sea-surface temperature (SST, not shown) are simulated to increase by $\sim 0.8\,^{\circ}C$ over the Holocene.

CPD
9, 1165–1235, 2013

In experiment CIRC, the global energy balance over the termination is strongly influenced by the enforced change in windstress and the simulated deglacial increase in SAT is almost twice as large in experiment CIRC than in BIO. This is a consequence of a much larger sea ice cover and a higher planetary albedo at LGM in experiment CIRC than BIO. Circulation is slow under the prescribed low glacial windstress and less heat is transported to high latitudes and less ice is exported from the Southern Ocean to lower latitudes in CIRC than BIO. In other words, the sea-ice-albedo feedback is much larger in CIRC than BIO.

Deep ocean ventilation evolves very differently in CIRC than in BIO (Fig. 6b). Here, we analyse the global average ^{14}C age difference of the deep ocean (i.e. waters below 2000 m depth) relative to the overlying surface ocean. The surface-to-deep age difference is recorded in ocean sediments as ^{14}C age offset between shells of benthic and planktonic (B-P) species. Results from the CTL experiment with time-invariant ocean ventilation show that this "proxy" is not an ideal age tracer; the B-P age difference is additionally influenced by transient atmospheric $\Delta^{14}C$ changes and varies between 600 and 1100 yr in CTL.

The wind stress forcing applied in experiment CIRC leads to an almost complete shut-down of the THC during the LGM and a recovery to Holocene values over the termination. Simulated B-P age increases from 2000 yr at LGM to peak at 2900 yr by 16.5 kyr BP. A slight and after 12 kyr BP a more pronounced decrease follows to the late Holocene B-P age of about 1000 yr. B-P variations are much smaller in simulation BIO, as no changes in windstress are applied; B-P age varies between 1000 and 1700 yr.

$\Delta\Delta^{14}C$, i.e. the global mean difference in $\Delta^{14}C$ between the deep ocean and the atmosphere is −500 ‰ in CIRC until Heinrich Stadial 1 (−350 ‰ in BIO), followed by a sharp increase of approx 150–200 ‰ and a slow relaxation to late-Holocene values (∼ −170 ‰). This behavior is also present in recently analyzed sediment cores, see e.g. Burke and Robinson (2012) and references therein. The sharp increase in $\Delta\Delta^{14}C$ following HS1 is mainly driven by the prescribed fast atmospheric drop.

CPD
9, 1165–1235, 2013

R. Roth and F. Joos

The forcings prescribed in our bounding experiments CIRC and BIO are broadly sufficient to reproduce the reconstructed deglacial CO_2 increase. This is evidenced by an analysis of the atmospheric carbon budget (Fig. 6d and f). In the control simulation (CTL) an addition of 1700 GtC is required to close the budget. In contrast, the mismatch in the budget is close to zero for BIO and about −100 GtC for CIRC at the end of the simulation. In other words, only small emissions from unknown origin have to be applied in average to close the budget. Both experiments need a CO_2 sink in the early Holocene as indicated by the negative missing emissions. Such a sink could have been carbon uptake of NH peatlands (Yu et al., 2010) as peatland-dynamics is not included in this model version. In summary, simulation CIRC corresponds to the picture of a slowly ventilated ocean during the LGM, whereas deep ocean ventilation changes remain small in BIO and are absent in the CTL simulation. The atmospheric carbon budget is approximately closed in simulations CIRC and BIO, whereas a substantial external carbon input is required in simulation CTL. These three simulations provide thus three radically different evolutions of the carbon cycle over the past 20 kyr and will serve us to assess uncertainties in inferred radiocarbon production rates due to our incomplete understanding of the past carbon cycle.

3.2.1 Time evolution of the radiocarbon production rate

Total inferred radiocarbon production, Q, varies between 350 and 650 mol yr^{-1} during the Holocene (Fig. 8d). Variations on multi-decadal to centennial time scales are typically within 100 mol yr^{-1}. The differences in Q in the early Holocene between the model setups CIRC, BIO, and CTL are mainly explained by offsets in the absolute value of Q, while the timing and magnitude of multi-decadal to centennial variations are very similar for the three setups. The absolute value of Q is about 40 mol yr^{-1} higher in CIRC than in BIO and about 60 mol yr^{-1} higher in CIRC than in CTL at 10 kyr BP. This difference becomes very small in the late Holocene and results are almost identical for CIRC and BIO after 4 kyr BP. Note that the absolute (preindustrial) value of the production rate is equal in all three setups per definition (see Eq. 1).

CPD
9, 1165–1235, 2013

The inferred Q is assigned according to Eq. (1) to individual contributions from a net ^{14}C fluxes from the atmosphere to the ocean ($^{14}F_{as}$), a net flux to the land ($^{14}F_{ab}$), and atmospheric loss terms (Fig. 8). Variations in these three terms contribute about equally to variations in Q on decadal-to-centennial timescales, whereas millennial scale variations in Q are almost entirely attributed to changes in $^{14}F_{as}$. This is in agreement with the results from the Fourier analysis presented in Sect. 3.1. Holocene and preindustrial mean fluxes and their temporal variance are listed in Table 2.

The oceanic component entering the calculation of Q is threefold (Fig. 9): (i) the compensation of the $DI^{14}C$ (and a small contribution of $DO^{14}C$) decay proportional to its inventory, (ii) changes in the inventory of ^{14}C itself mainly driven by F_{as} and (iii) the export, rain and subsequent burial of $Ca^{14}CO_3$ and $PO^{14}C$. Thus, the mentioned offset in $^{14}F_{as}$ between CIRC and BIO at the early Holocene are the result of differences in the dynamical evolution of the whole-ocean DIC inventories and its $\Delta^{14}C$ signature. During LGM conditions, the oceanic ^{14}C inventory is larger for BIO than CIRC as the deep ocean is more depleted in the slowly overturning ocean of setup CIRC. Accordingly the decay of ^{14}C and $^{14}F_{as}$ is higher in simulation BIO than in CIRC (Fig. 9). The simulated oceanic ^{14}C inventory decreases both in CIRC and BIO as the (prescribed) atmospheric $\Delta^{14}C$ decreases. However, this decrease is smaller in CIRC than in BIO as the enforced increase in the THC and in ocean ventilation in CIRC leads to an additional ^{14}C flux into the ocean. In addition, the strengthened ventilation leads to a peak in organic matter export and burial while the reduced remineralization depth in BIO leads to the opposite effect (as less POM is reaching the seafloor). In total, the higher oceanic radiocarbon decay in BIO is overcompensated by the (negative) change of the oceanic inventory. Enhanced sedimentary loss of ^{14}C in CIRC further increases the offset finally leading to a higher Q at 10 kyr BP of $\sim 40\,\mathrm{mol\,yr^{-1}}$ in CIRC than in BIO. This offset has vanished almost completely at 7 kyr BP, apart from a small contribution from sedimentary processes.

In general, the influence of climate induced carbon-cycle changes is modest in the Holocene. This is indicated by the very similar Q in the CTL experiment. The biggest

CPD
9, 1165–1235, 2013

discrepancy between results from CTL versus those from CIRC and BIO emerge during the industrial period. Q drops rapidly in CTL as the combustion of the radiocarbon-depleted fossil fuel is not explicitly included.

In a further sensitivity run, the influence of the interhemispheric $\Delta^{14}C$ gradient on Q is explored (Fig. 8e; dashed line). In simulation INT09 the Northern Hemisphere dataset IntCal09 is applied globally and all other forcings are as in BIO. Differences in Q between CIRC/BIO and INT09 are generally smaller than 20 $mol\,yr^{-1}$, but grow to 50 $mol\,yr^{-1}$ from 1900 to 1950 AD. The reason are the different slopes in the last decades of the northern and Southern Hemisphere record. This sensitivity experiment demonstrates that spatial gradients in atmospheric $\Delta^{14}C$ and in resulting radiocarbon fluxes should be taken into account using a spatially resolved model.

In conclusion, inferred Holocene values of Q and in particular decadal-to-centennial variation in Q are only weakly sensitive to the details of the carbon cycle evolution over the glacial termination. On the other hand spatial gradients in atmospheric $\Delta^{14}C$ and carbon emissions from fossil fuel burning should be explicitly included to estimate radiocarbon production in the industrial period. In the following, we will use the arithmetic mean of BIO and CIRC as our best estimate for Q (Fig. 10). The final record is filtered using smoothing splines (Enting, 1987) with a cutoff-period of 20 yr in order to remove high-frequency noise.

Total uncertainties in Q (Fig. 10, gray band) are estimated to be around ± 12 % ($\pm 1\sigma$) at 10 kyr BP and to slowly diminish to around ±3–4 % by 1800 AD (Appendix Fig. A1f). Overall uncertainty in Q increases over the industrial period and is estimated to be ± 9 % by 1950 AD.The difference in Q between BIO and CIRC is assumed to reflect the uncertainty range due to our incomplete understanding of the deglacial CO_2 evolution. Uncertainties in the $\Delta^{14}C$ input data, the air-sea gas exchange rate and the gross primary production (GPP) of the land biosphere are taken into account using a Monte-Carlo approach and based on further sensitivity simulations (see A1 for details of the error estimation).

CPD
9, 1165–1235, 2013

The radiocarbon production records from Usoskin and Kromer (2005) and from the Marmod09 box-model (http://www.radiocarbon.org/IntCal09%20files/marmod09.csv, model described in Hughen et al., 2004) show similar variations on timescales of decades to millennia (Fig. 10). These include maxima in Q during the well-documented solar minima of the last millennium, generally low production, pointing to high solar activity, during the Roman period, as well as a broad maximum around 7.5 kyr BP. However, the production estimates of Usoskin and Kromer (2005) and Marmod09 are about 10 % lower during the entire Holocene and are in general outside our uncertainty range. If we can rely on our data-based estimates of the total radiocarbon inventory in the Earth System, then the lower average production rate in the Usoskin and Kromer (2005) and Marmod09 records suggest that the radiocarbon inventory is underestimated in their setups.

In the industrial period, the Marmod09 production rate displays a drop in Q by almost a factor of two. This seems unrealistic in the context of earlier variation in Q and may point to an inadequate treatment of anthropogenic carbon emissions. Usoskin and Kromer (2005) does not provide data after 1900 AD.

3.2.2 A reference radiocarbon production rate

Next, we discuss the absolute value of Q in more detail. Averaged over the Holocene, our simulations yield a ^{14}C production of $Q = 472\,\mathrm{mol\,yr^{-1}}$ ($1.77\,\mathrm{atoms\,cm^{-2}\,s^{-1}}$) as listed in Table 2. Independent calculations of particle fluxes and cosmogenic radionuclide production rates (Masarik and Beer, 1999, 2009) estimate $Q = 2.05\,\mathrm{atoms\,cm^{-2}\,s^{-1}}$ (they state an uncertainty of 10 %) for a solar modulation potential of $\Phi = 550\,\mathrm{MeV}$. As already visible from Fig. 10, Usoskin and Kromer (2005) obtained an lower Holocene mean Q of $1.506\,\mathrm{atoms\,cm^{-2}\,s^{-1}}$. Recently, Kovaltsov et al. (2012) presented an alternative production model and reported an average production rate of $1.88\,\mathrm{atoms\,cm^{-2}\,s^{-1}}$ for the period 1750–1900 AD. This is higher than our estimate for the same period of $1.75\,\mathrm{atoms\,cm^{-2}\,s^{-1}}$. We compare absolute numbers of Q for different values of Φ (see next section) and the geomagnetic dipole moment

CPD
9, 1165–1235, 2013

(Fig. 13). To determine Q for any given VADM and Φ is not without problems because the probability that the modelled evolution hits any point in the (VADM,Φ)-space is small (Fig. 13). In addition, the value depends on the calculation and normalization of Φ which introduces another source of error.

For the present-day VADM and $\Phi = 550$ MeV (see Sect. 3.3), our carbon-cycle based estimate of Q is ~ 1.71 atoms $cm^{-2}\,s^{-1}$ and thus lower than the value reported by Masarik and Beer (2009). Note that the statistical uncertainty in our record becomes negligible in the calculation of the time-averaged Q. Systematic and structural uncertainties in the preindustrial data-based ocean radiocarbon inventory of approx. 15 % (Key et al., 2004) dominates the uncertainty in the mean production rate, while uncertainties in the terrestrial ^{14}C sink are of minor relevance. Therefore we estimate the total uncertainty of the base level of our production rate to be of order 15 %.

3.3 Results for the solar activity reconstruction

Next, we combine our production record Q with estimates of VADM to compute the solar modulation potential Φ with the help of the model output from Masarik and Beer (1999) which gives the slope in the Q-Φ space for a given value of VADM (we do not use their absolute values of Q). Uncertainties in Φ are again assessed using a Monte Carlo approach (see Appendix A2 for details on the different sources of uncertainty in Φ and TSI).

One key problem is the normalization of Φ, i.e. how Φ is aligned to observational data (Muscheler et al., 2007). The period of overlap of the Q record with ground-based measurements is very limited as uncertainties in the atmospheric injection of radiocarbon from atomic bomb tests hinders the determination of Q from the $\Delta^{14}C$ record after 1950 AD. Forbush ground-based ionization chamber (IC) data recently reanalyzed by Usoskin et al. (2011) (US11) are characterized by large uncertainties and only cover roughly one solar cycle (mid 1936–1950 AD). The considerable uncertainties both in Q and Φ in this period make it difficult to connect reconstructions of past solar activity to the recent epoch. Still, we choose to use these monthly data to normalize

CPD
9, 1165–1235, 2013

our record. Converting the LIS used for US11 to the one used by Castagnoli and Lal (1980) (which we use throughout this study) according to Herbst et al. (2010) yields an average solar modulation potential of $\Phi = 403$ MeV during our calibration epoch 1937–1950 AD. Accordingly, we normalize our Q-record such that (the monte-carlo mean) Φ equals 403 MeV for the present-day VADM and the period 1937 to 1950 AD. In this time period, the uncertainty in the IC data is ~ 140 MeV. In addition, the error due to uncertainties in Q is approx. 70 MeV. This makes it difficult to draw firm conclusion on the reliability of the normalization. Thus, the absolute magnitude of our reconstructed Φ remains uncertain.

We linearly blend the Q-based Φ with a 11 yr running mean of the monthly data from US11 in the overlap period 1937–1950 AD and extend the Reconstruction up to 2005 AD. Smoothing splines with a cutoff period of 20 yr are applied to remove high-frequency noise, e.g. as introduced by the MC ensemble averaging and the blending. This blending with instrumental data slightly changes the average Φ in 1937–1950 AD from 403 to ~ 420 MeV.

Φ varies during the Holocene between 100 and 1200 MeV on decadal-to-centennial time scales (Fig. 12) with a median value of approximately 570 MeV (see histogram in Fig. 13). Millennial-scale variations of Φ during the Holocene appear small (Fig. 12). This suggests that the millennial-scale variations in the radiocarbon production Q (Fig. 10) appear to be mainly driven by variations in the magnetic field of the Earth (Fig. 11). The millennial-scale modulation of Q is not completely removed when applying VADM of Korte et al. (2011). It is difficult to state whether the remaining long-term modulation, recently interpreted as a solar cycle (Xapsos and Burke, 2009), is of solar origin or rather related to uncertainties in reconstructed VADM.

Values around 670 MeV in the last 50 yr of our record (1955–2005 AD) indicate a high solar activity compared to the average Holocene conditions. However, such high values are not exceptional. Multiple periods with peak-to-peak variations 400–600 MeV occur throughout the last 10 000 yr, induced by so-called grand solar minima and maxima.

CPD
9, 1165–1235, 2013

The Sun's present state can be characterized by a grand solar maximum (modern maximum) with its peak in 1985 (Lockwood, 2010).

Our reconstruction of Φ is compared with those of Usoskin et al. (2007) (US07, converted to GM75 LIS), of Muscheler et al. (2007) (MEA07) and with the reconstruction of Steinhilber et al. (2008) (SEA08) who used the ice core record of ^{10}Be instead of radiocarbon data (Fig. 12). Overall, the agreement between the the ^{10}Be and the ^{14}C-based reconstructions points toward the quality of these proxies for solar reconstructions. In detail, differences remain. For example, the ^{14}C-based reconstructions show a increase in Φ in the second half of the 17th century, whereas the ^{10}Be -derived record suggest a decrease in Φ during this period.
In difference to SEA08, which is based on ^{10}Be ice core records, our Φ is always positive and non-zero and thus within the physically plausible range.

Solanki et al. (2004) suggests that solar activity is unusually high during recent decades compared to the values reconstructed for the entire Holocene. Our reconstruction does not point to an exceptionally high solar activity in recent decades in agreement with the conclusions of Muscheler et al. (2007). The relatively higher modern values inferred by Solanki et al. (2004) are eventually related to their application of a Northern Hemisphere Δ^{14}C dataset (IntCal98) only. Thus, these authors neglected the influence of interhemispheric differences in Δ^{14}C. We calculated Φ from results of our sensitivity simulation INT09, where the IntCal09 Northern Hemisphere data are applied globally. Due to the lower Q in the normalization period from 1937 to 1950 AD (see Fig. 8, dashed line), the Φ-record during the Holocene is shifted downward by approximately 150 MeV for INT09 compared to CIRC/BIO; the same normalization of Φ to the Forbush data is applied. Then, the solar activity for recent decades appears unusually high compared to Holocene values in the INT09 case.

3.4 Reconstructed total solar irradiance

We apply the reconstruction of Φ in combination with Eqs. (3) and (4) to reconstruct total solar irradiance TSI (Fig. 14). Uncertainties in TSI are again estimated using a Monte Carlo approach and considering uncertainties in Φ and in the parameters of the analytical relationship (but not the $\pm 0.4\,\mathrm{W\,m^{-2}}$ in the TSI-B_r-relationship) TSI is expressed as deviation from the solar cycle minimum in 1986, here taken to be $1365.57\,\mathrm{W\,m^{-2}}$. We note that recent measures suggest a slight downward revision of the absolute value of TSI by a few permil (Kopp and Lean, 2011); this hardly effect reconstructed TSI anomalies. The irradiance reduction during the Maunder Minimum is $0.85 \pm 0.17\,\mathrm{W\,m^{-2}}$ (1685 AD) compared to the solar cycle 22 average value of $1365.9\,\mathrm{W\,m^{-2}}$. This is a reduction in TSI of 0.62 ± 0.12 ‰ .

Changes in TSI can be expressed as radiative forcing (RF) which is given by $\Delta \mathrm{TSI} \times \frac{1}{4} \times (1 - A)$ where A is the Earth's mean albedo (~ 0.3). A reduction of $0.85\,\mathrm{W\,m^{-2}}$ corresponds to a change in RF of about $0.15\,\mathrm{W\,m^{-2}}$ only. This is more than an order of magnitude smaller than the current radiative forcing due to the anthropogenic CO_2 increase of $1.8\,\mathrm{W\,m^{-2}}$ ($5.35\,\mathrm{W\,m^{-2}}\ \ln(390\,\mathrm{ppm}/280\,\mathrm{ppm})$). This small reduction in TSI and RF is a direct consequence of the small slope in the relationship between TSI and the interplanetary magnetic field as suggested by Fröhlich (2009). Applying the relationships between TSI and Φ suggested by Shapiro et al. (2011) would yield almost an order of magnitude larger changes in TSI and RF.

We compare our newly produced TSI record with two other recently published reconstructions based on radionuclide production, Vieira et al. (2011) (VEA11) and Steinhilber et al. (2012) (SEA12). For the last millennium, the data from Delaygue and Bard (2011) (DB11) is shown for completeness. During three grand minima in the last millennium, i.e. the Wolf, Spörer and Maunder minima, SEA12 shows plateau-like values, apparently caused by a truncation of the Φ record to positive values. Also VEA11 suggests lower values during these minima compared to our record, but in general the differences in the TSI reconstructions are small, in particular when compared to the large TSI variations suggested by Shapiro et al. (2011).

Well known solar periodicities in TSI contain the Hallstatt (2300 yr), Eddy (1000 yr), Suess (210 yr) and de Vries cycle (70–100 yr) as also discussed by Wanner et al. (2008) and Lundstedt et al. (2006). These periodicities are also present in our

CPD
9, 1165–1235, 2013

Radiocarbon production and solar activity

R. Roth and F. Joos

reconstruction (Fig. 15), as well as the long-term modulation of approx. 6000 yr (Xapsos and Burke, 2009) (not shown). A wavelet (Morlet) power spectrum indicates that the power associated with the different cycles fluctuated somewhat during the Holocene.

We use the predictability of TSI given by its periodic nature to extrapolate insolation changes up to 2500 AD. The extrapolation is calculated using autogregressive (AR) modeling, applying the Burg method (Kay, 1988) (Fig. 15c). The order of the model is the number of years of the TSI record used to fit the model, for example 1000th order means that only the period 1005–2005 AD is used for fitting while the 10 000th order model takes the entire TSI record into account. Common to all extrapolations is the decreasing TSI in the next 10–20 yr to a magnitude comparable to 1900 AD. Towards 2200 AD, all three extrapolations show again increasing TSI.

3.5 Changes in global mean surface air temperature from total solar irradiance variability

We translate our new TSI record as well as two earlier reconstructions (VEA11, SEA12) into past changes in SAT using the Bern3D-LPX model. We follow the same protocol as in Sect. 2.2. Two transient simulations were performed for each TSI reconstruction: in one simulation TSI is kept constant at its mean value, in the other simulation the actual TSI reconstruction is applied. ΔSAT was then computed as the difference between the two simulations, normalized to ΔSAT = 0 °C in 2005 AD. As shown in Fig. 16, the three reconstructions yield rather small temperature changes attributed to solar forcing with |ΔSAT| less than 0.15 °C at any time during the Holocene. Compared to VEA12 and SEA12, our TSI reconstruction results in less negative and more positive values in ΔSAT before 1900 AD as expected from the TSI record. No considerable TSI-induced longterm temperature trend is simulated. We note that our energy balance model does not take into account spectral changes and changes in ultraviolet (UV) radiation and thus related heating or cooling of the stratosphere by the absorption of UV by ozone and other agents (Gray et al., 2010).

4 Summary and conclusions

In the present study the Holocene evolution of cosmogenic radiocarbon (^{14}C) production is reconstructed using a state of the art Earth System Model of Intermediate Complexity and the IntCal09/SHCal04 radiocarbon records. Then this production record is used in combinations with reconstructions of the geomagnetic field to reconstruct the solar modulation potential Φ. In further steps, total solar irradiance (TSI) is reconstructed using a recently proposed relationship between Φ and TSI and variations in TSI were translated into temperature anomalies. The uncertainty arising from uncertainties in input data, model parameterizations for the glacial termination, and model parameter values are propagated through the entire chain from production to solar modulation to TSI using Monte Carlo and sensitivity simulations as well as Gaussian error propagation.

The Bern3D-LPX model is used to estimate radiocarbon production from the IntCal09/SHCal04 radiocarbon records. The model features a 3-dimensional dynamic ocean component with an ocean sediment model and an interactive marine biological cycle, a 2-D atmosphere and a dynamic global vegetation model component. The model is able to reproduce the observation-based distributions of carbon and radiocarbon within the ocean as well as to approximate the evolution of atmospheric CO_2 during the past 20 ka. The explicit representation of dissolved inorganic carbon and dissolved inorganic radiocarbon and the biological cycle in a 3-dimensional dynamic setting is a step forward compared to the often applied perturbation approach with the box-diffusion model of Oeschger et al. (1975) or the outcrop model of Siegenthaler (1983) (Vieira et al., 2011; Usoskin and Kromer, 2005; Solanki et al., 2004; Muscheler et al., 2005b). These model underestimate by design the inventory of dissolved inorganic carbon in the ocean due to the neglect of the marine biological cycle. Thus, the marine radiocarbon inventory and implied cosmogenic production is also underestimated. The Bern3D-LPX carbon-climate model is forced with reconstructed changes in orbital parameters, ice sheet extent influencing surface albedo and in natural and

CPD
9, 1165–1235, 2013

anthropogenic variations in greenhouse gas concentrations and sulphate aerosol forcings and climate variations, thereby taking into account the influence of climatic variations on the cycling of carbon and radiocarbon.

Our production rate estimates can be compared to independent estimates obtained with models that compute production of cosmogenic nuclides in the atmosphere by simulating the interaction of incoming high energy particles with atmospheric molecules (Masarik and Beer, 1999, 2009). Masarik and Beer (2009) suggests a production of 2.05 ± 0.2 for a solar modulation potential of 550 MeV. The radiocarbon budget analysis yields a lower production of 1.71 atoms $cm^{-2} s^{-1}$ and for the same Φ. The Holocene mean ^{14}C production depends on variations in Φ and the geomagnetic field and is estimated to 1.77 atoms $cm^{-2} s^{-1}$.

An open question was by how much uncertainties in the carbon cycle processes leading to the deglacial CO_2 rise affect estimates of the radiocarbon production. To this end, two alternative, bounding scenarios for the deglacial CO_2 rise were applied in addition to a control simulations with constant climate and ocean circulation. We show that uncertainties in the processes responsible for the reconstructed CO_2 over the glacial termination translate into an uncertainty of order 5 % in the absolute magnitude of the production in the early Holocene, but only to small uncertainties in decadal-to-centennial production variations. This uncertainty in millennial average production due to the memory of the system to earlier changes vanishes over the Holocene and becomes very small (< 1 %) in recent millennia.

Small differences between simulations that include Holocene climate change and the control run with no climate change are found. A caveat is that our 2-dimensional atmospheric energy-moisture balance model does not represent important features of climate variability such as interannual and decadal atmospheric modes. However, the available evidence and the generally good agreement between ^{14}C-based and independent solar proxy reconstructions suggest that atmospheric radiocarbon and inferred production are relatively insensitive to typical Holocene climate variations.

CPD
9, 1165–1235, 2013

Solar modulation potential Φ is computed using the relationship between radiocarbon production, the geomagnetic dipole (Korte et al., 2011), and Φ from the Masarik and Beer (1999) model as in Muscheler et al. (2007). A key step is the normalization of the ^{14}C-derived Φ record to the Forbush instrumental observations over the period 1937 to 1950 AD. Atmospheric Δ^{14}C is heavily contaminated after 1950 by atomic bomb tests preventing a reliable extraction of the natural production signal. In the mid-20th century, atmospheric Δ^{14}C and its interhemispheric gradient is influenced by the early signals of fossil fuel combustion and land use. Our spatially-resolved model allows us to treat interhemispheric concentration differences and land use explicitly. We show that reconstructions in Φ that rely on the Northern Hemisphere Δ^{14}C record only are biased towards low values during the Holocene. To our knowledge, the Φ record by Usoskin et al. (2007) is based on Q from Usoskin and Kromer (2005) and thus on the Northern Hemisphere radiocarbon record only. Their values are systematically lower than ours and their best estimates are in general outside our 1σ confidence band during the last 7 ka. The Φ record by Steinhilber et al. (2008) shows in generally values below our confidence range during the period 7 to 3 kyr BP, while the two reconstructions agree on average during the more recent millennia. Agreement with respect to decadal-to-centennial variability is generally high among the different reconstructions. However, notable exceptions exist. For example, the reconstruction by Steinhilber et al. (2008) suggest a strong negative fluctuation between 8 and 7.8 kyr BP, not seen in the ^{14}C-derived records.

We reevaluated the claim by Solanki et al. (2004) that the recent Sun is exceptionally active. As earlier studies (Muscheler et al., 2007; Steinhilber et al., 2008), we conclude that recent solar activity is high but not unusual in the context of the Holocene. Φ was estimated to be on average at 650 MeV during the last 25 yr by Steinhilber et al. (2008) and for a reference Local Interstellar Spectrum (LIS) of Castagnoli and Lal (1980). We find an average Φ for the Holocene (9 to 0 kyr BP) of 560 MeV. Solar activity in our decadally-smoothed record is during 28 % of the time higher than the modern average of 650 MeV and during 40 % higher than 600 MeV, used to define periods of high

CPD
9, 1165–1235, 2013

activity by Steinhilber et al. (2008) (Fig. 13). This may be compared to corresponding values of 2 and 15 % by Steinhilber et al. (2008). In contrast to earlier reconstructions, our record suggests that periods of high solar activity (> 600 MeV) were quite common not only in recent millennia but throughout the Holocene.

Our reconstruction in Φ can be used to derive a range of solar irradiance reconstructions using published method. Shapiro et al. (2011) suggest that variations in spectral and thus total solar irradiance (TSI) are proportional to variation in Φ. Their analysis suggest a high scaling of Φ with TSI and a Maunder Minimum reduction in TSI compared to present solar minimum by about 0.4 %. This is significantly larger than the reduction suggested in other recent reconstructions (Steinhilber et al., 2012; Vieira et al., 2011), but within the range of TSI variations explored in earlier climate model studies (Ammann et al., 2007; Jansen et al., 2007). Here, we further converted Φ into TSI using the nonlinear equations used by Steinhilber et al. (2008). This yields small variations in TSI and a Maunder Minimum reduction in TSI compared to recent solar minima of only 0.62 ‰. The resulting overall range in TSI is about 1.2 $\mathrm{W\,m^{-2}}$. Future extension of TSI using autoregressive modeling suggest a declining solar activity in the next decades towards average Holocene conditions.

We applied different TSI reconstructions to estimate variations in global mean surface air temperature (SAT) due to TSI changes only. We stress that these SAT anomalies are due to TSI variations only and do not include SAT variations due to other drivers such as orbital forcing, natural and anthropogenic greenhouse gas concentration variations, or changes in the extent and the albedo of ice sheets. The results suggest that there were several periods in the Holocene were TSI-related SAT anomalies were larger than for year 2000 AD. In particular, several warm anomalies occurred in the period from 5500 to 3600 BP. Temperature anomalies are comparable to twenty century anomalies in the period from 200 BC to 600 AD. In contrast, the TSI reconstruction of Steinhilber et al. (2012) implies that SAT anomalies due to TSI changes were below current values almost during the entire Holocene. In conclusion, our reconstruction of

CPD
9, 1165–1235, 2013

the radiocarbon production rate and the solar modulation potential and implied changes in solar irradiance provide an alternative for climate modellers.

Appendix A

Estimation of uncertainties

A1 Assessment of uncertainties in the ^{14}C production record

There are several potential sources of errors entering the calculation of the production rate, summarized in Fig. A1. As already discussed in detail in the main text, the uncertain deglacial carbon-cycle changes translates into an uncertainty in Q especially in the early Holocene. To account for this, we use the arithmetic mean of BIO and CIRC as our best guess Q reconstruction and the difference between them as uncertainty range which is around 3 % in the early Holocene and drops below 1 % in 5000 BP.

In addition, also the uncertainty of the IntCal09/SHCal04-record translates into an error of the production record. 100 radiocarbon histories were randomly generated with Gaussian distributed $\Delta^{14}C$ values at each point in time of the record (varied within their 1σ uncertainty as shown in Fig. 2b). For each realization of the $\Delta^{14}C$ history the transient simulation with Bern3D-LPX was repeated. The 1σ range of these resulting production rates (Fig. A1b) is in the order of 8–10 % decreasing towards preindustrial times to 3 %. During 1930–1950, this error increases again rapidly (hardly visible in Fig. A1b) from 3 to 10 % because the atmospheric carbon inventory increases at a high rate. Therefore, rather small errors in $\Delta^{14}C$ of ~ 1 ‰ translate into rather big uncertainties in the change of the atmospheric radiocarbon inventory, and thus into the production rate.

The air–sea flux of radiocarbon is the dominant flux out of the atmosphere with approx. 430 mol yr^{-1}. We assess its variations by nominally changing the air-sea gas-exchange rate within ± 15 % (Müller et al., 2008). Two additional runs were performed

CPD
9, 1165–1235, 2013

in which the seasonally and spatially varying gas exchange rates of the standard setup were increased/decreased everywhere by 15 %. In analogy, uncertainties in the flux into the land biosphere were assessed by varying the gross primary productivity of the model by ±15 %. In these two experiments, differences in the total ^{14}C inventory were subtracted to get the uncertainties in the fluxes alone, the effect of the inventory is discussed separately. These errors in $^{14}F_{as} + ^{14}F_{ab}$ vary together with changes in the atmospheric $\Delta^{14}C$ signature. The error from the uncertainty in the combined air-to-sea and air-to-land ($^{14}F_{as} + ^{14}F_{ab}$) fluxes is smaller than 2.5 % of the production at any time (Fig. A1d).

Uncertainties are also related to the ^{14}C signature associated with the carbon flux applied to close the atmospheric CO_2 budget ($^{14}F_{budget}$ in Eq. 1). For example, of the missing carbon sink process could be due to a slow down of the oceanic thermohaline circulation (THC) or a growth of land vegetation: two processes with different isotopic signatures. We assume that this signature varies between ±200 ‰ relative to the contemporary atmosphere. The associated error in the production is in general small with peaks of 1–2 % (Fig. A1e). However, towards 1950 AD, where the anthropogenic influence leads to increasing CO_2 levels, the uncertainty reaches up to 4 % as the model simulates a too weak oceanic/land-sink and/or too high emissions.

In summary, the total uncertainty in the production rate is dominated by the uncertainty in the $\Delta^{14}C$ input data. We estimate the total standard deviation by quadratic error addition $\sigma_Q = \sqrt{\sum \sigma_{Q,i}^2}$ to be ~ 12 % during the early Holocene decreasing to 3–4 % towards preindustrial times (Fig. A1f). In the first half of the last century, uncertainties increase again mainly associated with the anthropogenic CO_2 increase. This increasing uncertainty towards 1950 AD (~ 9 %) is important when normalizing reconstructed solar modulation to the recent instrumental records.

CPD
9, 1165–1235, 2013

Title Page
Abstract Introduction
Conclusions References
Tables Figures
Back Close
Full Screen / Esc
Printer-friendly Version
Interactive Discussion

A2 Propagation of uncertainties from Q to Φ and ΔTSI

Next, the uncertainty calculation of Φ (Fig. 12, grey band) and of ΔTSI (Fig. 14) is discussed. Three general sources of uncertainty in Φ are considered: the uncertainty in Q, the uncertainty in VADM and finally the error of the production rate simulations (i.e. the slope of Φ/Q) assumed to be 10 %. Using Monte Carlo calculations, we varied the different sources of uncertainty individually to assess the propagation of errors. In Fig. A2b–d the individual 1σ errors of this calculation is shown. Note that the uncertainty of VADM vanishes towards 1950 as the dipole moment is normalized relative to the modern value. The total error in Φ varies then between 350 MeV (early Holocene) and 80 MeV (preindustrial). The potential error introduced by the normalization is not included in this figure. This would add another 100 MeV uncertainty to the average level of Φ, but not on its preindustrial temporal evolution. The uncertainty in Q is the main source of the uncertainty in Φ.

Similarly, the uncertainty in the change in TSI as reconstructed with the help of Eqs. (3) and (4) is calculated (Fig. A3b and c). The 1σ error of Φ is taken into account as well as the uncertainties in Eq. (4) and of the exponent α in Eq. (3) (±0.3) (Steinhilber et al., 2009). The error in the reference value of TSI (1264.64 $\mathrm{W\,m^{-2}}$ in Eq. 4) does not affect relative changes in TSI, but its absolute level. The total 1σ uncertainty in ΔTSI ranges between 0.2–0.8 $\mathrm{W\,m^{-2}}$ (Fig. A3d), to equal part stemming from the error in Φ and the conversion model.

Acknowledgements. We would like to thank M. Korte for providing VADM data, I. Usoskin for the production rate data and F. Steinhilber for providing help with the Φ/TSI calculation methods. This work is supported by the Swiss National Science Foundation through the National Centre for Competence in Research NCCR-climate and by the grant to Climate and Environmental Physics and support by the European Commission through the FP7 projects Past4Future (grant no. 243908) and CARBOCHANGE (grant no. 264879).

CPD
9, 1165–1235, 2013

References

Adkins, J., Griffin, S., Kashgarian, M., Cheng, H., Druffel, E., Boyle, E., Edwards, R., and Shen, C.: Radiocarbon dating of deep-sea corals, Radiocarbon, 44, 567–580, 2002. 1175

Ammann, C. M., Joos, F., Schimel, D. S., Otto-Bliesner, B. L., and Tomas, R. A.: Solar influence on climate during the past millennium: results from transient simulations with the NCAR Climate System Model, P. Natl. Acad. Sci. USA, 104, 3713–3718, doi:10.1073/pnas.0605064103, 2007. 1167, 1198

Anderson, R. F., Ali, S., Bradtmiller, L. I., Nielsen, S. H. H., Fleisher, M. Q., Anderson, B. E., and Burckle, L. H.: Wind-driven upwelling in the Southern Ocean and the deglacial rise in atmospheric CO_2, Science, 323, 1443–1448, doi:10.1126/science.1167441, 2009. 1175

Andres, R., Fielding, D., Marland, G., Boden, T., Kumar, N., and Kearney, A.: Carbon dioxide emissions from fossil-fuel use, 1751–1950, Tellus B, 51, 759–765, doi:10.1034/j.1600-0889.1999.t01-3-00002.x, 1999. 1174

Antonov, J. I., Seidov, D., Boyer, T. P., Locarnini, R. A., Mishonov, A. V., Garcia, H. E., Baranova, O. K., Zweng, M. M., and Johnson, D. R.: World Ocean Atlas 2009, Vol. 2: Salinity, NOAA Atlas NESDIS 68, US Government Printing Office, Washington, D.C., 2010. 1178

Bard, E., Raisbeck, G., Yiou, F., and Jouzel, J.: Solar modulation of cosmogenic nuclide production over the last millennium: comparison between C-14 and Be-10 records, Earth Planet. Sc. Lett., 150, 453–462, doi:10.1016/S0012-821X(97)00082-4, 1997. 1168

Bard, E., Raisbeck, G., Yiou, F., and Jouzel, J.: Solar irradiance during the last 1200 years based on cosmogenic nuclides, Tellus B, 52, 985–992, doi:10.1034/j.1600-0889.2000.d01-7.x, 2000. 1170

Bauer, J. E., Williams, P. M., and Druffel, E. R. M.: ^{14}C activity of dissolved organic carbon fractions in the north-central Pacific and Sargasso Sea, Nature, 357, 667–670, doi:10.1038/357667a0, 1992. 1178

Beer, J., Andrée, M., Oeschger, H., Stauffer, B., Balzer, R., Bonani, G., Stoller, C., Suter, M., Wölfli, W., and Finkel, R. C.: Temporal ^{10}Be variations in ice, Radiocarbon, 25, 269–278, 1983. 1168

Berger, A. L.: Long-term variations of daily insolation and quaternary climatic changes, J. Atmos. Sci., 35, 2362–2367, 1978. 1174

Discussion Paper | Discussion Paper | Discussion Paper | Discussion Paper |

CPD

9, 1165–1235, 2013

Radiocarbon production and solar activity

R. Roth and F. Joos

Title Page
Abstract Introduction
Conclusions References
Tables Figures
◀ ▶
Back Close
Full Screen / Esc
Printer-friendly Version
Interactive Discussion

Bouttes, N., Paillard, D., Roche, D. M., Brovkin, V., and Bopp, L.: Last Glacial Maximum CO_2 and $\delta^{13}C$ successfully reconciled, Geophys. Res. Lett., 38, L02705, doi:10.1029/2010GL044499, 2011. 1175

Brovkin, V., Ganopolski, A., Archer, D., and Rahmstorf, S.: Lowering of glacial atmospheric CO_2 in response to changes in oceanic circulation and marine biogeochemistry, Paleoceanography, 22, PA4202, doi:10.1029/2006PA001380, 2007. 1175

Brovkin, V., Ganopolski, A., Archer, D., and Munhoven, G.: Glacial CO_2 cycle as a succession of key physical and biogeochemical processes, Clim. Past, 8, 251–264, doi:10.5194/cp-8-251-2012, 2012. 1169

Bryan, S. P., Marchitto, T. M., and Lehman, S. J.: The release of ^{14}C-depleted carbon from the deep ocean during the last deglaciation: evidence from the Arabian Sea, Earth Planet. Sc. Lett., 298, 244–254, doi:10.1016/j.epsl.2010.08.025, 2010. 1176

Burke, A. and Robinson, L. F.: The Southern Ocean's role in carbon exchange during the last deglaciation, Science, 335, 557–561, doi:10.1126/science.1208163, 2012. 1175, 1185

Castagnoli, G. and Lal, D.: Solar modulation effects in terrestrial production of carbon-14, Radiocarbon, 22, 133–158, 1980. 1191, 1197, 1228

Clark, P. U., Shakun, J. D., Baker, P. A., Bartlein, P. J., Brewer, S., Brook, E., Carlson, A. E., Cheng, H., Kaufman, D. S., Liu, Z., Marchitto, T. M., Mix, A. C., Morrill, C., Otto-Bliesner, B. L., Pahnke, K., Russell, J. M., Whitlock, C., Adkins, J. F., Blois, J. L., Clark, J., Colman, S. M., Curry, W. B., Flower, B. P., He, F., Johnson, T. C., Lynch-Stieglitz, J., Markgraf, V., McManus, J., Mitrovica, J. X., Moreno, P. I., and Williams, J. W.: Global climate evolution during the last deglaciation, P. Natl. Acad. Sci. USA, 109, E1134–E1142, doi:10.1073/pnas.1116619109, 2012. 1175

Crowley, T. J.: Causes of climate change over the past 1000 years, Science, 289, 270–277, doi:10.1126/science.289.5477.270, 2000. 1167, 1174

Delaygue, G. and Bard, E.: An Antarctic view of beryllium-10 and solar activity for the past millennium, Clim. Dynam., 36, 2201–2218, doi:10.1007/s00382-010-0795-1, 2011. 1174, 1193, 1230

De Pol-Holz, R., Keigwin, L., Southon, J., Hebbeln, D., and Mohtadi, M.: No signature of abyssal carbon in intermediate waters off Chile during deglaciation, Nat. Geosci., 3, 192–195, doi:10.1038/ngeo745, 2010. 1176

CPD
9, 1165–1235, 2013
Radiocarbon production and solar activity
R. Roth and F. Joos

Edwards, N. R. and Marsh, R.: Uncertainties due to transport-parameter sensitivity in an efficient 3-D ocean-climate model, Clim. Dynam., 24, 415–433, doi:10.1007/s00382-004-0508-8, 2005. 1172

Elsig, J., Schmitt, J., Leuenberger, D., Schneider, R., Eyer, M., Leuenberger, M., Joos, F., Fischer, H., and Stocker, T. F.: Stable isotope constraints on Holocene carbon cycle changes from an Antarctic ice core, Nature, 461, 507–510, doi:10.1038/nature08393, 2009. 1174

Enting, I. G.: On the use of smoothing splines to filter CO_2 data, J. Geophys. Res., 92, 10977–10984, doi:10.1029/JD092iD09p10977, 1987. 1182, 1188

Farquhar, G. D., Caemmerer, S. V., and Berry, J. A.: A biochemical-model of photosynthetic CO_2 assimilation in leaves of C-3 species, Planta, 149, 78–90, 1980. 1173

Feely, R., Sabine, C., Lee, K., Berelson, W., Kleypas, J., Fabry, V., and Millero, F.: Impact of anthropogenic CO_2 on the $CaCO_3$ system in the oceans, Science, 305, 362–366, doi:10.1126/science.1097329, 2004. 1215

Francey, R., Allison, C., Etheridge, D., Trudinger, C., Enting, I., Leuenberger, M., Langenfelds, R., Michel, E., and Steele, L.: A 1000-year high precision record of δ^{13}C in atmospheric CO_2, Tellus B, 51, 170–193, doi:10.1034/j.1600-0889.1999.t01-1-00005.x, 1999. 1174

Franois, R., Altabet, M. A., Yu, E.-F., Sigman, D. M., Bacon, M. P., Frank, M., Bohrmann, G., Bareille, G., and Labeyrie, L. D.: Contribution of Southern Ocean surface-water stratification to low atmospheric CO_2 concentrations during the last glacial period, Nature, 389, 929–935, doi:10.1038/40073, 1997. 1175

Fröhlich, C.: Evidence of a long-term trend in total solar irradiance, Astron. Astrophys., 501, L27–L30, doi:10.1051/0004-6361/200912318, 2009. 1181, 1193

Galbraith, E. D., Jaccard, S. L., Pedersen, T. F., Sigman, D. M., Haug, G. H., Cook, M., Southon, J. R., and Francois, R.: Carbon dioxide release from the North Pacific abyss during the last deglaciation, Nature, 449, 890–893, doi:10.1038/nature06227, 2007. 1175

Gehlen, M., Bopp, L., Emprin, N., Aumont, O., Heinze, C., and Ragueneau, O.: Reconciling surface ocean productivity, export fluxes and sediment composition in a global biogeochemical ocean model, Biogeosciences, 3, 521–537, doi:10.5194/bg-3-521-2006, 2006. 1173

Gerber, S., Joos, F., Brugger, P., Stocker, T. F., Mann, M. E., Sitch, S., and Scholze, M.: Constraining temperature variations over the last millennium by comparing simulated and observed atmospheric CO_2, Clim. Dynam., 20, 281–299, doi:10.1007/s00382-002-0270-8, 2003. 1173

Gleeson, L. and Axford, W.: Solar modulation of galactic cosmic rays, Astrophys. J., 154, 1011–1026, doi:10.1086/149822, 1968. 1180

Gray, L. J., Beer, J., Geller, M., Haigh, J. D., Lockwood, M., Matthes, K., Cubasch, U., Fleitmann, D., Harrison, G., Hood, L., Luterbacher, J., Meehl, G. A., Shindell, D., van Geel, B., and White, W.: Solar influences on climate, Rev. Geophys., 48, RG4001, doi:10.1029/2009RG000282, 2010. 1167, 1194

Griffies, S. M.: The Gent–Williams skew flux, J. Phys. Oceanogr., 28, 831–841, doi:10.1175/1520-0485(1998)028<0831:TGMSF>2.0.CO;2, 1998. 1172

Hambaryan, V. V. and Neuhäuser, R.: A galactic short gamma-ray burst as cause for the ^{14}C peak in AD 774/5, Mon. Not. R. Astron. Soc., doi:10.1093/mnras/sts378, in press, 2013. 1180

Hansell, D. A., Carlson, C. A., Repeta, D. J., and Schlitzer, R.: Dissolved organic matter in the ocean a controversy stimulates new insights, Oceanography, 22, 202–211, 2009. 1178, 1215

Heinze, C., Maier-Reimer, E., Winguth, A. M. E., and Archer, D.: A global oceanic sediment model for long-term climate studies, Global Biogeochem. Cy., 13, 221–250, 1999. 1173

Herbst, K., Kopp, A., Heber, B., Steinhilber, F., Fichtner, H., Scherer, K., and Matthiä, D.: On the importance of the local interstellar spectrum for the solar modulation parameter, J. Geophys. Res., 115, D00I20, doi:10.1029/2009JD012557, 2010. 1191, 1228

Hodell, D. A., Venz, K. A., Charles, C. D., and Ninnemann, U. S.: Pleistocene vertical carbon isotope and carbonate gradients in the South Atlantic sector of the Southern Ocean, Geochem. Geophy. Geosys., 4, 1–19, doi:10.1029/2002GC000367, 2003. 1175

Hughen, K., Baillie, M., Bard, E., Beck, J., Bertrand, C., Blackwell, P., Buck, C., Burr, G., Cutler, K., Damon, P., Edwards, R., Fairbanks, R., Friedrich, M., Guilderson, T., Kromer, B., McCormac, G., Manning, S., Ramsey, C., Reimer, P., Reimer, R., Remmele, S., Southon, J., Stuiver, M., Talamo, S., Taylor, F., van der Plicht, J., and Weyhenmeyer, C.: Marine04 marine radiocarbon age calibration, 0–26 cal kyr BP, Radiocarbon, 46, 1059–1086, 2004. 1189

Jackson, A., Jonkers, A. R. T., and Walker, M. R.: Four centuries of geomagnetic secular variation from historical records, Philos. T. Roy. Soc. A, 358, 957–990, doi:10.1098/rsta.2000.0569, 2000. 1180, 1227

Jansen, E., Overpeck, J., Briffa, K. R., Duplessy, J.-C., Joos, F., Masson-Delmotte, V., Olago, D., Otto-Bliesner, B., Peltier, W. R., Rahmstorf, S., Ramesh, R., Raynaud, D., Rind, D., Solomina, O., Villalba, R., and Zhang, D.: Palaeoclimate, in: Climate Change 2007: The Physical Science Basis. Working Group I Contribution to the Fourth Assessment Report of the

Intergovernmental Panel on Climate Change, edited by: Solomon, S., Qin, D., Manning, M., Chen, Z., Marquis, M., Averyt, K. B., Tignor, M., and Miller, H. L., Cambridge University Press, 433–497, 2007. 1198

Joos, F. and Spahni, R.: Rates of change in natural and anthropogenic radiative forcing over the past 20,000 years, P. Natl. Acad. Sci. USA, 105, 1425–1430, doi:10.1073/pnas.0707386105, 2008. 1174

Joos, F., Prentice, I. C., Sitch, S., Meyer, R., Hooss, G., Plattner, G.-K., Gerber, S., and Hasselmann, K.: Global warming feedbacks on terrestrial carbon uptake under the Intergovernmental Panel on Climate Change (IPCC) emission scenarios, Global Biogeochem. Cy., 15, 891–907, 2001. 1173, 1174

Joos, F., Gerber, S., Prentice, I. C., Otto-Bliesner, B. L., and Valdes, P. J.: Transient simulations of Holocene atmospheric carbon dioxide and terrestrial carbon since the Last Glacial Maximum, Global Biogeochem. Cy., 18, GB2002, doi:10.1029/2003GB002156, 2004. 1173

Jungclaus, J. H., Lorenz, S. J., Timmreck, C., Reick, C. H., Brovkin, V., Six, K., Segschneider, J., Giorgetta, M. A., Crowley, T. J., Pongratz, J., Krivova, N. A., Vieira, L. E., Solanki, S. K., Klocke, D., Botzet, M., Esch, M., Gayler, V., Haak, H., Raddatz, T. J., Roeckner, E., Schnur, R., Widmann, H., Claussen, M., Stevens, B., and Marotzke, J.: Climate and carbon-cycle variability over the last millennium, Clim. Past, 6, 723–737, doi:10.5194/cp-6-723-2010, 2010. 1167

Kalnay, E., Kanamitsu, M., Kistler, R., Collins, W., Deaven, D., Gandin, L., Iredell, M., Saha, S., White, G., Woollen, J., Zhu, Y., Chelliah, M., Ebisuzaki, W., Higgins, W., Janowiak, J., Mo, K., Ropelewski, C., Wang, J., Leetmaa, A., Reynolds, R., Jenne, R., and Joseph, D.: The NCEP/NCAR 40-year reanalysis project, B. Am. Meteorol. Soc., 77, 437–471, doi:10.1175/1520-0477(1996)077<0437:TNYRP>2.0.CO;2, 1996. 1172

Kay, S. M.: Modern Spectral Estimation: Theory and Application, Prentice-Hall, Englewood Cliffs, N.J., 1988. 1194

Key, R. M., Kozyr, A., Sabine, C. L., Lee, K., Wanninkhof, R., Bullister, J. L., Feely, R. A., Millero, F. J., Mordy, C., and Peng, T.-H.: A global ocean carbon climatology: results from Global Data Analysis Project (GLODAP), Global Biogeochem. Cy., 18, GB4031, doi:10.1029/2004GB002247, 2004. 1170, 1173, 1178, 1190, 1215

Klein Goldewijk, K.: Estimating global land use change over the past 300 years: the HYDE database, Global Biogeochem. Cy., 15, 417–433, 2001. 1174

CPD
9, 1165–1235, 2013

Radiocarbon production and solar activity

R. Roth and F. Joos

Title Page
Abstract Introduction
Conclusions References
Tables Figures
◀ ▶
Back Close
Full Screen / Esc
Printer-friendly Version
Interactive Discussion

Klein Goldewijk, K. and van Drecht, G.: HYDE3: current and historical population and land cover, in: Integrated Modelling of Global Environmental Change, An Overview of IMAGE 2.4., edited by: Bouwman, A. F., Kram, T., and Klein Goldewijk, K., Netherlands Environmental Assessment Agency (MNP), Bilthoven, The Netherlands, 2006. 1174

Knudsen, M. F., Riisager, P., Donadini, F., Snowball, I., Muscheler, R., Korhonen, K., and Pesonen, L. J.: Variations in the geomagnetic dipole moment during the Holocene and the past 50 kyr, Earth Planet. Sc. Lett., 272, 319–329, doi:10.1016/j.epsl.2008.04.048, 2008. 1170, 1180, 1227

Köhler, P., Fischer, H., Munhoven, G., and Zeebe, R.: Quantitative interpretation of atmospheric carbon records over the last glacial termination, Global Biogeochem. Cy., 19, GB4020, doi:10.1029/2004GB002345, 2005. 1175

Kopp, G. and Lean, J. L.: A new, lower value of total solar irradiance: evidence and climate significance, Geophys. Res. Lett., 38, L01706, doi:10.1029/2010GL045777, 2011. 1193

Korte, M., Constable, C., Donadini, F., and Holme, R.: Reconstructing the Holocene geomagnetic field, Earth Planet. Sc. Lett., 312, 497–505, doi:10.1016/j.epsl.2011.10.031, 2011. 1167, 1170, 1180, 1191, 1197, 1227, 1228, 1234

Kovaltsov, G. A., Mishev, A., and Usoskin, I. G.: A new model of cosmogenic production of radiocarbon ^{14}C in the atmosphere, Earth Planet. Sc. Lett., 337–338, 114–120, doi:10.1016/j.epsl.2012.05.036, 2012. 1166, 1169, 1189

Krakauer, N. Y., Randerson, J. T., Primeau, F. W., Gruber, N., and Menemenlis, D.: Carbon isotope evidence for the latitudinal distribution and wind speed dependence of the air–sea gas transfer velocity, 7th International Carbon Dioxide Conference (CO_2), Boulder, CO, 25–30 September 2005, Tellus B, 58, 390–417, doi:10.1111/j.1600-0889.2006.00223.x, 2006. 1172

Kwon, E. Y., Primeau, F., and Sarmiento, J. L.: The impact of remineralization depth on the air–sea carbon balance, Nat. Geosci., 2, 630–635, doi:10.1038/ngeo612, 2009. 1176

Lambert, F., Delmonte, B., Petit, J. R., Bigler, M., Kaufmann, P. R., Hutterli, M. A., Stocker, T. F., Ruth, U., Steffensen, J. P., and Maggi, V.: Dust-climate couplings over the past 800,000-years from the EPICA Dome C ice core, Nature, 452, 616–619, doi:10.1038/nature06763, 2008. 1174

Lean, J.: Evolution of the Sun's spectral irradiance since the Maunder Minimum, Geophys. Res. Lett., 27, 2425–2428, doi:10.1029/2000GL000043, 2000. 1170

CPD
9, 1165–1235, 2013

Radiocarbon production and solar activity

R. Roth and F. Joos

Lisiecki, L. E. and Raymo, M. E.: A Pliocene-Pleistocene stack of 57 globally distributed benthic δ^{18}O records, Paleoceanography, 20, PA1003, doi:10.1029/2004PA001071, 2005. 1174

Locarnini, R. A., Mishonov, A. V., Antonov, J. I., Boyer, T. P., Garcia, H. E., Baranova, O. K., Zweng, M. M., and Johnson, D. R.: World Ocean Atlas 2009, Vol. 1: Temperature, NOAA Atlas NESDIS 68, US Government Printing Office, Washington, D.C., 2010. 1178

Lockwood, M.: Solar change and climate: an update in the light of the current exceptional solar minimum, P. Natl. Acad. Sci. USA, 466, 303–329, doi:10.1098/rspa.2009.0519, 2010. 1192

Lockwood, M.: Solar influence on global and regional climates, Surv. Geophys., 33, 503–534, doi:10.1007/s10712-012-9181-3, 2012. 1167

Lockwood, M. and Owens, M. J.: Centennial changes in the heliospheric magnetic field and open solar flux: the consensus view from geomagnetic data and cosmogenic isotopes and its implications, J. Geophys. Res., 116, A04109, doi:10.1029/2010JA016220, 2011. 1168

Lundstedt, H., Liszka, L., Lundin, R., and Muscheler, R.: Long-term solar activity explored with wavelet methods, Ann. Geophys., 24, 769–778, doi:10.5194/angeo-24-769-2006, 2006. 1193

Luo, C., Mahowald, N. M., and del Corral, J.: Sensitivity study of meteorological parameters on mineral aerosol mobilization, transport, and distribution, J. Geophys. Res., 108, 4447, doi:10.1029/2003JD003483, 2003. 1174

MacFarling Meure, C., Etheridge, D., Trudinger, C., Steele, P., Langenfelds, R., van Ommen, T., Smith, A., and Elkins, J.: Law Dome CO_2, CH_4 and N_2O ice core records extended to 2000 years BP, Geophys. Res. Lett., 33, L14810, doi:10.1029/2006GL026152, 2006. 1215

Mahowald, N. M., Muhs, D. R., Levis, S., Rasch, P. J., Yoshioka, M., Zender, C. S., and Luo, C.: Change in atmospheric mineral aerosols in response to climate: last glacial period, preindustrial, modern, and doubled carbon dioxide climates, J. Geophys. Res., 111, D10202, doi:10.1029/2005JD006653, 2006. 1174

Marchal, O.: Optimal estimation of atmospheric ^{14}C production over the Holocene: paleoclimate implications, Clim. Dynam., 24, 71–88, doi:10.1007/s00382-004-0476-z, 2005. 1167, 1169

Marchitto, T. M., Lehman, S. J., Ortiz, J. D., Fluckiger, J., and van Geen, A.: Marine radiocarbon evidence for the mechanism of deglacial atmospheric CO_2 rise, Science, 316, 1456–1459, 2007. 1176

Masarik, J. and Beer, J.: Simulation of particle fluxes and cosmogenic nuclide production in the Earth's atmosphere, J. Geophys. Res., 104, 12099–12111, doi:10.1029/1998JD200091, 1999. 1169, 1180, 1189, 1190, 1196, 1197

Masarik, J. and Beer, J.: An updated simulation of particle fluxes and cosmogenic nuclide production in the Earth's atmosphere, J. Geophys. Res., 114, D11103, doi:10.1029/2008JD010557, 2009. 1166, 1169, 1189, 1190, 1196

Matsumoto, K.: Biology-mediated temperature control on atmospheric $p\mathrm{CO}_2$ and ocean biogeochemistry, Geophys. Res. Lett., 34, L20605, doi:10.1029/2007GL031301, 2007. 1176

McCormac, F., Hogg, A., Blackwell, P., Buck, C., Higham, T., and Reimer, P.: SHCal04 Southern Hemisphere calibration, 0–11.0 cal kyr BP, Radiocarbon, 46, 1087–1092, 2004. 1167, 1168, 1174, 1175, 1215, 1218

Menviel, L. and Joos, F.: Toward explaining the Holocene carbon dioxide and carbon isotope records: results from transient ocean carbon cycle-climate simulations, Paleoceanography, 27, PA1207, doi:10.1029/2011PA002224, 2012. 1175

Menviel, L., Joos, F., and Ritz, S.: Simulating atmospheric CO_2, ^{13}C and the marine carbon cycle during the Last Glacial-Interglacial cycle: possible role for a deepening of the mean remineralization depth and an increase in the oceanic nutrient inventory, Quaternary Sci. Rev., 56, 46–68, doi:10.1016/j.quascirev.2012.09.012, 2012. 1169, 1175, 1176

Miyake, F., Nagaya, K., Masuda, K., and Nakamura, T.: A signature of cosmic-ray increase in ad 774–775 from tree rings in Japan, Nature, 486, 240–242, doi:10.1038/nature11123, 2012. 1180

Monnin, E., Steig, E. J., Siegenthaler, U., Kawamura, K., Schwander, J., Stauffer, B., Stocker, T. F., Morse, D. L., Barnola, J.-M., Bellier, B., Raynaud, D., and Fischer, H.: Evidence for substantial accumulation rate variability in Antarctica during the Holocene, through synchronization of CO_2 in the Taylor Dome, Dome C and DML ice cores, Earth Planet. Sc. Lett., 224, 45–54, doi:10.1016/j.epsl.2004.05.007, 2004. 1218

Müller, S. A., Joos, F., Edwards, N. R., and Stocker, T. F.: Water mass distribution and ventilation time scales in a cost-efficient, three-dimensional ocean model, J. Climate, 19, 5479–5499, doi:10.1175/JCLI3911.1, 2006. 1170, 1171, 1172

Müller, S. A., Joos, F., Edwards, N. R., and Stocker, T. F.: Modeled natural and excess radiocarbon: sensitivities to the gas exchange formulation and ocean transport strength, Global Biogeochem. Cy., 22, GB3011, doi:10.1029/2007GB003065, 2008. 1170, 1172, 1199

Muscheler, R., Beer, J., Kubik, P. W., and Synal, H.-A.: Geomagnetic field intensity during the last 60,000 years based on ^{10}Be and ^{36}Cl from the Summit ice cores and ^{14}C, Quaternary Sci. Rev., 24, 1849–1860, 2005a. 1169

Muscheler, R., Joos, F., Muller, S. A., and Snowball, I.: Climate: how unusual is today's solar activity?, Nature, 436, E3–E4, :doi10.1038/nature04045, 2005b. 1167, 1195

Muscheler, R., Joos, F., Beer, J., Müller, S. A., Vonmoos, M., and Snowball, I.: Solar activity during the last 1000 yr inferred from radionuclide records, Quaternary Sci. Rev., 26, 82–97, doi:10.1016/j.quascirev.2006.07.012, 2007. 1168, 1180, 1190, 1192, 1197, 1228

Muscheler, R., Kromer, B., Bjorck, S., Svensson, A., Friedrich, M., Kaiser, K. F., and Southon, J.: Tree rings and ice cores reveal ^{14}C calibration uncertainties during the Younger Dryas, Nat. Geosci., 1, 263–267, doi:10.1038/ngeo128, 2008. 1168

Naegler, T. and Levin, I.: Closing the global radiocarbon budget 1945–2005, J. Geophys. Res.-Atmos., 111, D12311, doi:10.1029/2005JD006758, 2006. 1170, 1172

Najjar, R. G., Orr, J., Sabine, C. L., and Joos, F.: Biotic-HOWTO, Internal OCMIP Report, Tech. rep., LSCE/CEA Saclay, Gif-sur-Yvette, France, 1999. 1172

Oeschger, H., Siegenthaler, U., Schotterer, U., and Gugelmann, A.: A box diffusion model to study the carbon dioxide exchange in nature, Tellus, 27, 168–192, 1975. 1169, 1195

Orr, J. and Najjar, R. G.: Abiotic-HOWTO, Internal OCMIP Report, Tech. rep., LSCE/CEA Saclay, Gif-sur-Yvette, France, 1999. 1172

Parekh, P., Joos, F., and Müller, S. A.: A modeling assessment of the interplay between aeolian iron fluxes and iron-binding ligands in controlling carbon dioxide fluctuations during Antarctic warm events, Paleoceanography, 23, PA4202, doi:10.1029/2007PA001531, 2008. 1171, 1172

Peltier, W. R.: Ice age paleotopography, Science, 265, 195–201, 1994. 1172, 1174

Peltier, W. R.: Global glacial isostasy and the surface of the ice-age Earth: the ICE-5G (VM2) model and GRACE, Annu. Rev. Earth Pl. Sc., 32, 111–149, doi:10.1146/annurev.earth.32.082503.144359, 2004. 1174

Reader, M. C. and Boer, G. J.: The modification of greenhouse gas warming by the direct effect of sulphate aerosols, Clim. Dynam., 14, 593–607, 1998. 1174

Reimer, P. J., Baillie, M. G. L., Bard, E., Bayliss, A., Beck, J. W., Blackwell, P. G., Ramsey, C. B., Buck, C. E., Burr, G. S., Edwards, R. L., Friedrich, M., Grootes, P. M., Guilderson, T. P., Hajdas, I., Heaton, T. J., Hogg, A. G., Hughen, K. A., Kaiser, K. F., Kromer, B., McCormac, F. G., Manning, S. W., Reimer, R. W., Richards, D. A., Southon, J. R., Talamo, S., Turney, C. S. M., van der Plicht, J., and Weyhenmeye, C. E.: IntCal09 and Marine09 radiocarbon age calibration curves, 0–50,000 years cal BP, Radiocarbon, 51, 1111–1150, 2009. 1167, 1168, 1174, 1175, 1215, 1218

CPD
9, 1165–1235, 2013

Radiocarbon production and solar activity

R. Roth and F. Joos

Ritz, S. P., Stocker, T. F., and Joos, F.: A coupled dynamical ocean-energy balance atmosphere model for paleoclimate studies, J. Climate, 24, 349–75, doi:10.1175/2010JCLI3351.1, 2011. 1171, 1172, 1173

Sarmiento, J. L. and Gruber, N.: Ocean Biogeochemical Dynamics, Chapt. 8: Carbon Cycle, Princeton University Press, 318–358, 2006. 1215

Schmidt, G. A., Jungclaus, J. H., Ammann, C. M., Bard, E., Braconnot, P., Crowley, T. J., Delaygue, G., Joos, F., Krivova, N. A., Muscheler, R., Otto-Bliesner, B. L., Pongratz, J., Shindell, D. T., Solanki, S. K., Steinhilber, F., and Vieira, L. E. A.: Climate forcing reconstructions for use in PMIP simulations of the last millennium (v1.0), Geosci. Model Dev., 4, 33–45, doi:10.5194/gmd-4-33-2011, 2011. 1167, 1181

Schmidt, G. A., Jungclaus, J. H., Ammann, C. M., Bard, E., Braconnot, P., Crowley, T. J., Delaygue, G., Joos, F., Krivova, N. A., Muscheler, R., Otto-Bliesner, B. L., Pongratz, J., Shindell, D. T., Solanki, S. K., Steinhilber, F., and Vieira, L. E. A.: Climate forcing reconstructions for use in PMIP simulations of the Last Millennium (v1.1), Geosci. Model Dev., 5, 185–191, doi:10.5194/gmd-5-185-2012, 2012. 1167

Schmitt, J., Schneider, R., Elsig, J., Leuenberger, D., Lourantou, A., Chappellaz, J., Köhler, P., Joos, F., Stocker, T. F., Leuenberger, M., and Fischer, H.: Carbon isotope constraints on the deglacial CO_2 rise from ice cores, Science, 336, 711–714, doi:10.1126/science.1217161, 2012. 1174, 1175

Scholze, M., Kaplan, J. O., Knorr, W., and Heimann, M.: Climate and interannual variability of the atmosphere-biosphere $^{13}CO_2$ flux, Geophys. Res. Lett., 30, 1097, doi:10.1029/2002GL015631, 2003. 1173

Schrijver, C. J., Livingston, W. C., Woods, T. N., and Mewaldt, R. A.: The minimal solar activity in 2008–2009 and its implications for long-term climate modeling, Geophy. Res. Lett., 38, L06701, doi:10.1029/2011GL046658, 2011. 1170

Shackleton, N.: Climate change across the hemispheres, Science, 291, 58–59, doi:10.1126/science.10.1126/SCIENCE.1057253, 2001. 1175

Shapiro, A. I., Schmutz, W., Rozanov, E., Schoell, M., Haberreiter, M., Shapiro, A. V., and Nyeki, S.: A new approach to the long-term reconstruction of the solar irradiance leads to large historical solar forcing, Astron. Astrophys., 529, A67, doi:10.1051/0004-6361/201016173, 2011. 1167, 1170, 1171, 1181, 1193, 1198

Siegenthaler, U.: Uptake of excess CO_2 by an outcrop-diffusion model of the ocean, J. Geophys. Res., 88, 3599–3608, 1983. 1169, 1195

Singarayer, J. S. and Valdes, P. J.: High-latitude climate sensitivity to ice-sheet forcing over the last 120 kyr, Quaternary Sci. Rev., 29, 43–55, doi:10.1016/j.quascirev.2009.10.011, 2010. 1174

Sitch, S., Smith, B., Prentice, I., Arneth, A., Bondeau, A., Cramer, W., Kaplan, J., Levis, S., Lucht, W., Sykes, M., Thonicke, K., and Venevsky, S.: Evaluation of ecosystem dynamics, plant geography and terrestrial carbon cycling in the LPJ dynamic global vegetation model, Global Change Biol., 9, 161–185, doi:10.1046/j.1365-2486.2003.00569.x, 2003. 1171, 1173

Skinner, L. C., Fallon, S., Waelbroeck, C., Michel, E., and Barker, S.: Ventilation of the deep Southern Ocean and deglacial CO_2 rise, Science, 328, 1147–1151, 2010. 1176

Solanki, S., Usoskin, I., Kromer, B., Schussler, M., and Beer, J.: Unusual activity of the Sun during recent decades compared to the previous 11,000 years, Nature, 431, 1084–1087, 2004. 1167, 1192, 1195, 1197

Spahni, R., Joos, F., Stocker, B. D., Steinacher, M., and Yu, Z. C.: Transient simulations of the carbon and nitrogen dynamics in northern peatlands: from the Last Glacial Maximum to the 21st century, Clim. Past Discuss., 8, 5633–5685, doi:10.5194/cpd-8-5633-2012, 2012. 1184

Steinacher, M.: Modeling Changes in the Global Carbon Cycle-Climate System, Ph. D. thesis, University of Bern, 2011. 1174

Steinhilber, F., Abreu, J. A., and Beer, J.: Solar modulation during the Holocene, Astrophys. Space Sci. T., 4, 1–6, doi:10.5194/astra-4-1-2008, 2008. 1180, 1192, 1197, 1198, 1228

Steinhilber, F., Beer, J., and Fröhlich, C.: Total solar irradiance during the Holocene, Geophys. Res. Lett., 36, L19704, doi:10.1029/2009GL040142, 2009. 1170, 1171, 1180, 1181, 1201

Steinhilber, F., Abreu, J. A., Beer, J., and McCracken, K. G.: Interplanetary magnetic field during the past 9300 years inferred from cosmogenic radionuclides, J. Geophys. Res., 115, A01104, doi:10.1029/2009JA014193, 2010. 1180

Steinhilber, F., Abreu, J. A., Beer, J., Brunner, I., Christl, M., Fischer, H., Heikkilä, U., Kubik, P. W., Mann, M., McCracken, K. G., Miller, H., Miyahara, H., Oerter, H., and Wilhelms, F.: 9,400 years of cosmic radiation and solar activity from ice cores and tree rings, P. Natl. Acad. Sci. USA, 109, 5967–5971, doi:10.1073/pnas.1118965109, 2012. 1167, 1168, 1169, 1170, 1180, 1193, 1198, 1230

Stocker, B. D., Strassmann, K., and Joos, F.: Sensitivity of Holocene atmospheric CO_2 and the modern carbon budget to early human land use: analyses with a process-based model, Biogeosciences, 8, 69–88, doi:10.5194/bg-8-69-2011, 2011. 1173

CPD
9, 1165–1235, 2013

Strassmann, K. M., Joos, F., and Fischer, G.: Simulating effects of land use changes on carbon fluxes: past contributions to atmospheric CO_2 increases and future commitments due to losses of terrestrial sink capacity, Tellus B, 60, 583–603, doi:10.1111/j.1600-0889.2008.00340.x, 2008. 1173
Stuiver, M. and Polach, H. A.: Discussion: reporting of ^{14}C data, Radiocarbon, 3, 355–363, 1977. 1169
Sweeney, C., Gloor, E., Jacobson, A. R., Key, R. M., McKinley, G., Sarmiento, J. L., and Wanninkhof, R.: Constraining global air-sea gas exchange for CO_2 with recent bomb ^{14}C measurements, Global Biogeochem. Cy., 21, GB2015, doi:10.1029/2006GB002784, 2007. 1170, 1172
Tagliabue, A., Bopp, L., Roche, D. M., Bouttes, N., Dutay, J.-C., Alkama, R., Kageyama, M., Michel, E., and Paillard, D.: Quantifying the roles of ocean circulation and biogeochemistry in governing ocean carbon-13 and atmospheric carbon dioxide at the last glacial maximum, Clim. Past, 5, 695–706, doi:10.5194/cp-5-695-2009, 2009. 1175
Tarnocai, C., Canadell, J. G., Schuur, E. A. G., Kuhry, P., Mazhitova, G., and Zimov, S.: Soil organic carbon pools in the northern circumpolar permafrost region, Global Biogeochem. Cy., 23, GB2023, doi:10.1029/2008GB003327, 2009. 1215
Thompson, S. L. and Warren, S. G.: Parameterization of outgoing infrared radiation derived from detailed radiative calculations, J. Atmos. Sci., 39, 2667–2680, 1982. 1172
Thornalley, D. J. R., Barker, S., Broecker, W. S., Elderfield, H., and McCave, I. N.: The deglacial evolution of North Atlantic deep convection, Science, 331, 202–205, doi:10.1126/science.1196812, 2011. 1176
Tschumi, T., Joos, F., and Parekh, P.: How important are Southern Hemisphere wind changes for low glacial carbon dioxide? A model study, Paleoceanography, 23, PA4208, doi:10.1029/2008PA001592, 2008. 1171
Tschumi, T., Joos, F., Gehlen, M., and Heinze, C.: Deep ocean ventilation, carbon isotopes, marine sedimentation and the deglacial CO_2 rise, Clim. Past, 7, 771–800, doi:10.5194/cp-7-771-2011, 2011. 1171, 1172, 1173, 1175, 1176, 1177
Usoskin, I. G. and Kromer, B.: Reconstruction of the C-14 production rate from measured relative abundance, Radiocarbon, 47, 31–37, 2005. 1167, 1169, 1183, 1189, 1195, 1197, 1226
Usoskin, I. G., Solanki, S. K., and Kovaltsov, G. A.: Grand minima and maxima of solar activity: new observational constraints, Astron. Astrophys., 471, 301–309, doi:10.1051/0004-6361:20077704, 2007. 1192, 1197, 1228

CPD
9, 1165–1235, 2013

Usoskin, I. G., Bazilevskaya, G. A., and Kovaltsov, G. A.: Solar modulation parameter for cosmic rays since 1936 reconstructed from ground-based neutron monitors and ionization chambers, J. Geophys. Res., 116, A02104, doi:10.1029/2010JA016105, 2011. 1190, 1228, 1229

Vecsei, A. and Berger, W. H.: Increase of atmospheric CO_2 during deglaciation: constraints on the coral reef hypothesis from patterns of deposition, Global Biogeochem. Cy., 18, GB1035, doi:10.1029/2003GB002147, 2004. 1174

Vieira, L. E. A., Solanki, S. K., Krivova, N. A., and Usoskin, I.: Evolution of the solar irradiance during the Holocene, Astron. Astrophys., 531, A6, doi:10.1051/0004-6361/201015843, 2011. 1167, 1180, 1193, 1195, 1198, 1230

Vonmoos, M., Beer, J., and Muscheler, R.: Large variations in Holocene solar activity: constraints from ^{10}Be in the Greenland Ice Core Project ice core, J. Geophys. Res., 111, A10105, doi:10.1029/2005JA011500, 2006. 1169

Wang, Y.-M., Lean, J. L., and Sheeley Jr., N. R.: Modeling the Sun's magnetic field and irradiance since 1713, Astrophys. J., 625, 522–538, 2005. 1170, 1174

Wanner, H., Beer, J., Crowley, T. J., Cubasch, U., Flückiger, J., Goosse, H., Grosjean, M., Joos, F., Kaplan, J. O., Küttel, M., Solomina, O., Stocker, T. F., Tarasov, P., Wagner, M., and Widmann, M.: Mid- to Late Holocene climate change: an overview, Quaternary Sci. Rev., 27, 1791–1828, doi:10.1016/j.quascirev.2008.06.013, 2008. 1193

Watson, R.: IPCC Special Report: Land Use, Land Use Change, and Forestry, Summary for Policymakers, Tech. rep., Cambridge University Press, New York, 2000. 1215

Weaver, A. J., Eby, M., Wiebe, E. C., Bitz, C. M., Duffy, P. B., Ewen, T. L., Fanning, A. F., Holland, M. M., MacFadyen, A., Wang, H. X., and Yoshimori, M.: The UVic Earth System Climate Model: model description, climatology, and applications to past, present and future climates, Atmos. Ocean, 39, 361–428, 2001. 1172

Xapsos, M. and Burke, E.: Evidence of 6000 year periodicity in reconstructed sunspot numbers, Sol. Phys., 257, 363–369, doi:10.1007/s11207-009-9380-3, 2009. 1191, 1194

Yang, S., Odah, H., and Shaw, J.: Variations in the geomagnetic dipole moment over the last 12000 years, Geophys. J. Int., 140, 158–162, doi:10.1046/j.1365-246x.2000.00011.x, 2000. 1180, 1227

Yu, Z., Loisel, J., Brosseau, D. P., Beilman, D. W., and Hunt, S. J.: Global peatland dynamics since the Last Glacial Maximum, Geophys. Res. Lett., 37, L13402, doi:10.1029/2010GL043584, 2010. 1184, 1186, 1215

CPD

9, 1165–1235, 2013

Radiocarbon production and solar activity

R. Roth and F. Joos

Title Page
Abstract Introduction
Conclusions References
Tables Figures
◀| |▶
◀ ▶
Back Close
Full Screen / Esc
Printer-friendly Version
Interactive Discussion

Table 1. Preindustrial model versus data based carbon and ^{14}C inventory estimates. The model-based oceanic inventories are calculated as the average of the experiments BIO and CIRC.

	Bern3D-LPX		Data	
	Carbon [Gt C]	^{14}C [10^5 mol]	Carbon [Gt C]	^{14}C [10^5 mol]
ATM	593	0.591	593[a]	0.591[b]
LND	1930	1.79	2500–3500[c]	
OCN	38 070	32.0	38 200[d]	33.00[d]
	Carbon [Gt C yr^{-1}]	^{14}C [mol yr^{-1}]	Carbon [Gt C yr^{-1}]	^{14}C [mol yr^{-1}]
SED	0.501	52	0.22–0.4[e]	

[a] MacFarling Meure et al. (2006).
[b] McCormac et al. (2004); Reimer et al. (2009).
[c] Watson (2000); Tarnocai et al. (2009); Yu et al. (2010).
[d] Key et al. (2004); Hansell et al. (2009).
[e] Sarmiento and Gruber (2006); Feely et al. (2004).

CPD
9, 1165–1235, 2013

Table 2. The atmospheric radiocarbon budget (positive numbers: loss of ^{14}C) averaged over the last 10 kyr and for preindustrial times (1750–1900 AD). The statistical uncertainty becomes negligible due to the averaging over hundreds of datapoints and is not given here. Instead, we report $\sqrt{VAR}$ (where VAR is the variance in time) to quantify the temporal variability of the corresponding fluxes. The bulk uncertainty in the time-averaged fluxes can be estimated by the uncertainty in the corresponding radiocarbon reservoirs and is of order 15 % except for the atmospheric component which is tightly constrained by data.

^{14}C loss [mol]	Holocene (10–0 kyr BP) best guess	$\sqrt{VAR}$	Preindustrial (1750–1900 AD) best guess	$\sqrt{VAR}$
$^{14}F_{as}$	436	27	451	33
$^{14}F_{ab}$	25	25	−6.9	47
ATM	11	23	24	44
total	472	57	468	35

Discussion Paper | Discussion Paper | Discussion Paper | Discussion Paper |
CPD
9, 1165–1235, 2013
Radiocarbon production and solar activity
R. Roth and F. Joos
Title Page
Abstract Introduction
Conclusions References
Tables Figures
◂ ▸
Back Close
Full Screen / Esc
Printer-friendly Version
Interactive Discussion

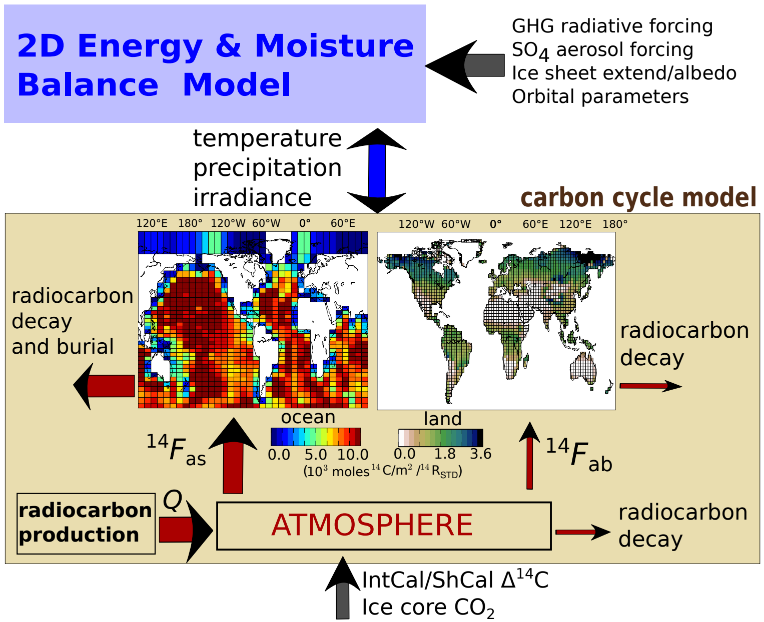

Fig. 1. Setup of the Bern3D-LPX carbon-cycle-climate model. Gray arrows denote externally applied forcings resulting from variations in greenhouse gas concentrations and aerosol loading, orbital parameters, ice sheet extent, sea level and atmospheric CO_2 and $\Delta^{14}C$. The atmospheric EBM model (blue box and arrows) communicates interactively calculated temperature, precipitation and irradiance to the carbon cycle model (light brown box). The production and exchange fluxes of radiocarbon within the carbon cycle model are sketched by red arrows, where the width of the arrows indicates the magnitude of the corresponding fluxes in a preindustrial steady state. The two maps show the depth-integrated inventories of the preindustrial ^{14}C content in the ocean and land modules.

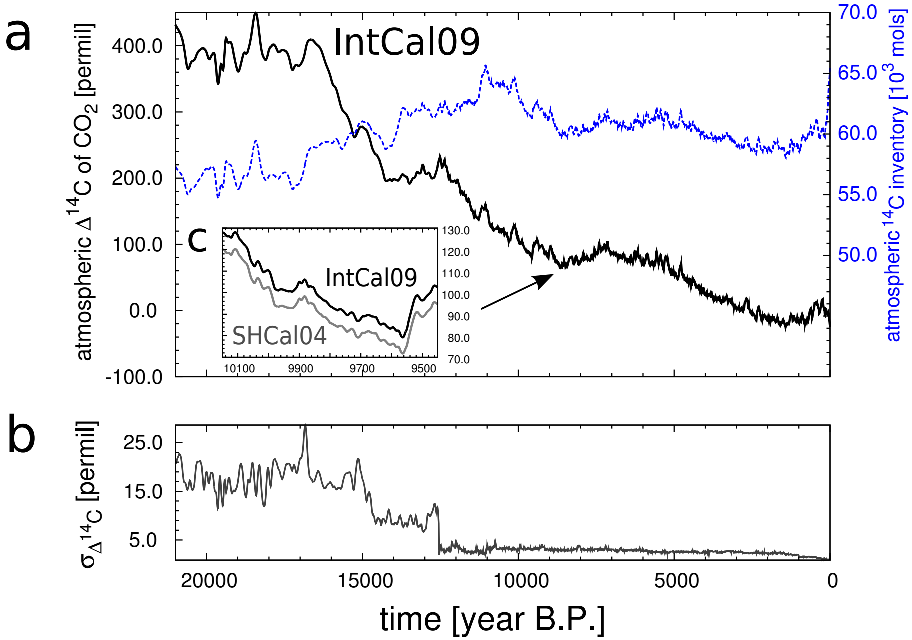

Fig. 2. (a) Reconstructed atmospheric $\Delta^{14}C$ of CO_2 (black, left axis) and the atmospheric radiocarbon inventory (blue, right axis) over the past 21 kyr. From 21 to 11 kyr BP radiocarbon data are from IntCal09 (Reimer et al., 2009). Afterward, we use IntCal09 data for the Northern Hemisphere and SHCal04 (McCormac et al., 2004) for the Southern Hemisphere, thereby taking into account the inter-hemispheric gradient of approx. 8‰ and hemisphere-specific anthropogenic depletion of ^{14}C during the industrial period. The two records are not distinguishable in this figure because of their proximity – see **(c)** for a zoom-in. The atmospheric radiocarbon inventory is computed from the $\Delta^{14}C$ records and the CO_2 record from Monnin et al. (2004). **(b)** The 1σ error assigned to the $\Delta^{14}C$ record and used as input for the Monte-Carlo uncertainty analysis.

CPD
9, 1165–1235, 2013

Radiocarbon production and solar activity

R. Roth and F. Joos

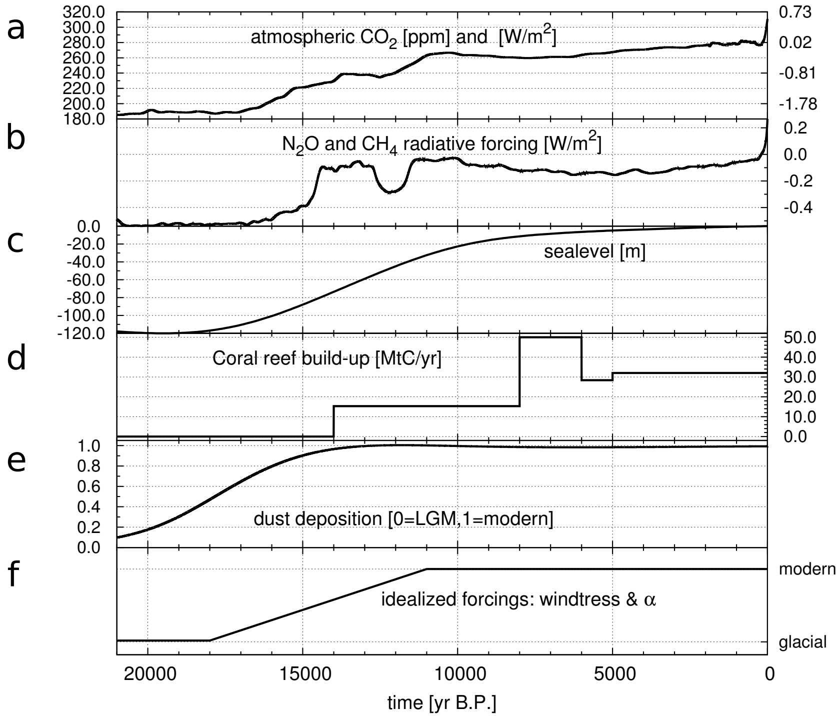

Fig. 3. Main forcings affecting the (preindustrial) Holocene carbon cycle. For completeness, the timeseries are shown starting from the LGM, i.e. the starting point of our transient simulations. **(a)** Atmospheric CO_2 used both for the radiative forcing as well as for the biogeochemical code, **(b)** radiative forcing of CH_4 and N_2O reported as deviation from preindustrial values, **(c)** sea-level record, **(d)** shallow water carbonate deposition, **(e)** (smoothed and normalized) EDC dust record to interpolate between LGM and modern dust deposition fields and **(f)** hypothetical windstress/remineralisation-depth forcings used for experiments CIRC/BIO. The reader is referred to the main text for details and references to the individual forcing components.

CPD
9, 1165–1235, 2013

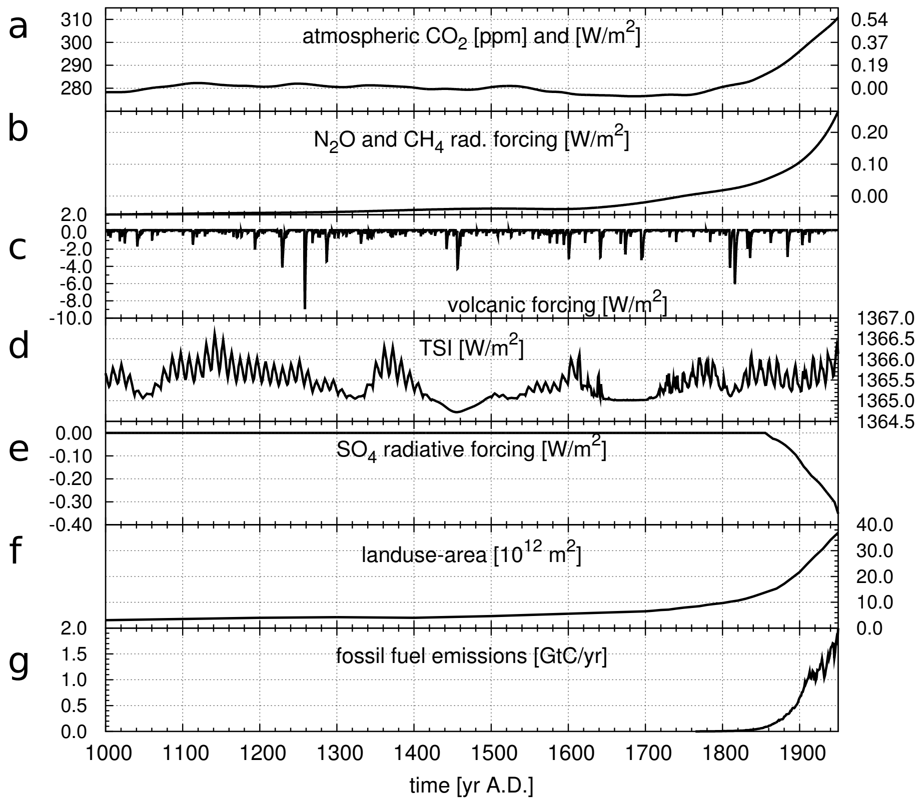

Fig. 4. Forcings for the industrial period: **(a)** atmospheric CO_2 used both for the radiative forcing as well as for the biogeochemical code, **(b)** radiative forcing of CH_4 and N_2O reported as deviation from preindustrial values, **(c)** volcanic forcing, **(d)** solar forcing, **(e)** SO_4 radiative forcing, **(f)** anthropogenic land use-area and **(g)** carbon emissions from fossil fuel use (including cement production). The reader is referred to the main text for details and references to the individual forcing components.

CPD
9, 1165–1235, 2013

Radiocarbon production and solar activity

R. Roth and F. Joos

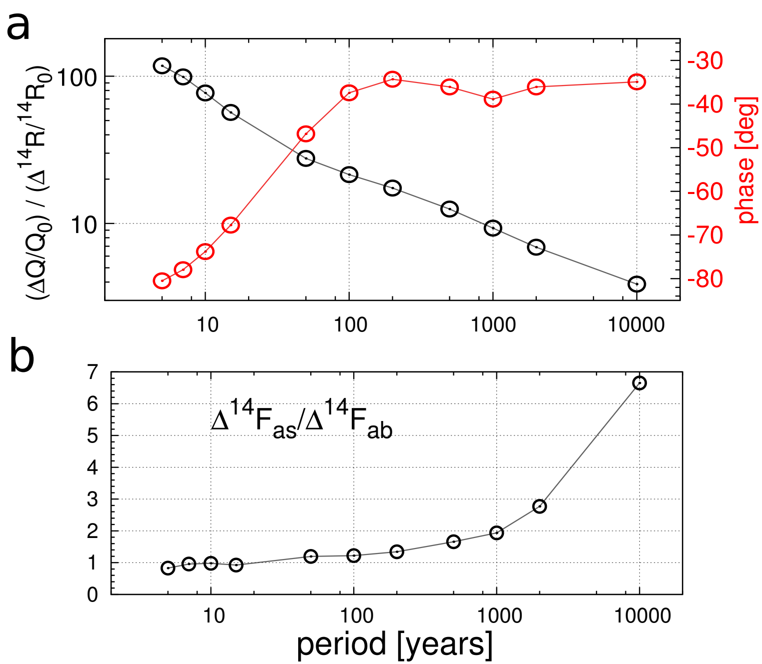

Fig. 5. Response of the Bern3D-LPX model to periodic sinusoidal variations in the atmospheric radiocarbon ratio (^{14}R) with an amplitude of 10‰ (in units of $\Delta^{14}C$). **(a)** Relative change in production rate, Q, divided by the relative change in ^{14}R (w.r.t. to a PI steady-state; black) and the phase shift between Q and ^{14}R (red, left axis); Q is always leading atmospheric ^{14}R. **(b)** Relative changes in the net atmosphere-to-sea (F_{as}) and the net atmosphere-to-land biosphere (F_{ab}) fluxes of ^{14}C for the same simulations.

CPD
9, 1165–1235, 2013

Radiocarbon production and solar activity

R. Roth and F. Joos

Title Page
Abstract
Introduction
Conclusions
References
Tables
Figures
◀
▶
Back
Close
Full Screen / Esc
Printer-friendly Version
Interactive Discussion

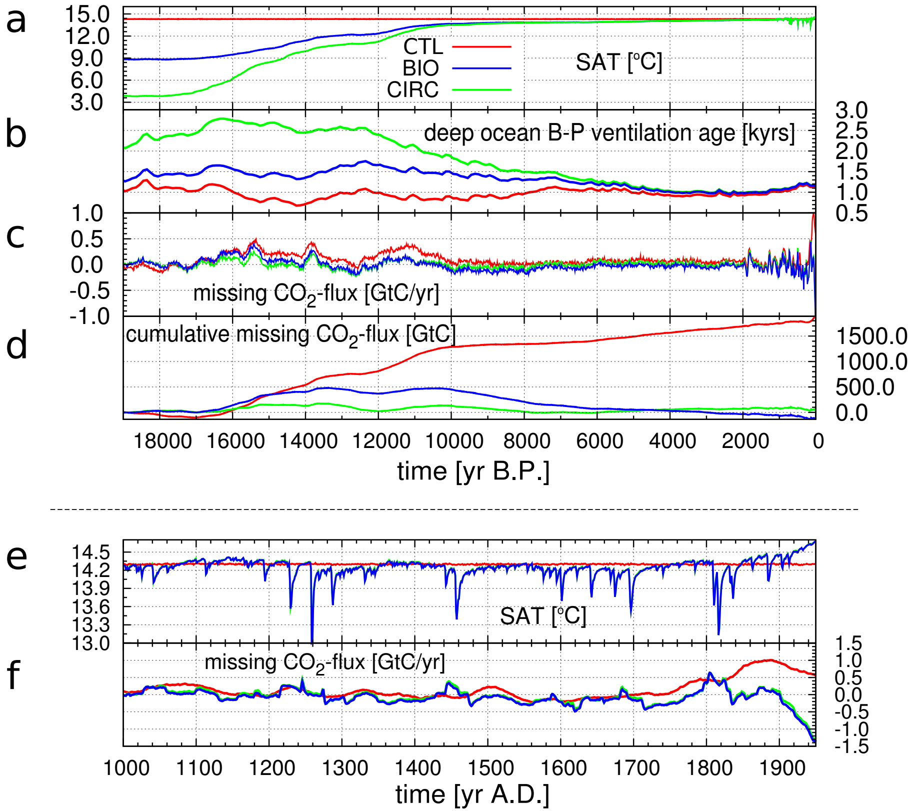

Fig. 6. Transient model response of **(a)** surface atmospheric temperature (SAT), **(b)** global averaged B-P reservoir age calculated as ^{14}C-age offset from the global ocean below 2000 m relative to the overlying surface ocean, **(c)** implied carbon flux to solve the atmospheric budget (F_{budget}) and cumulative sum thereof **(d)** for the experiments BIO, CIRC and the control-run CTL. For the last millennium, SAT and F_{budget} is shown in detail in the lower two panels **(e, f)**.

CPD
9, 1165–1235, 2013

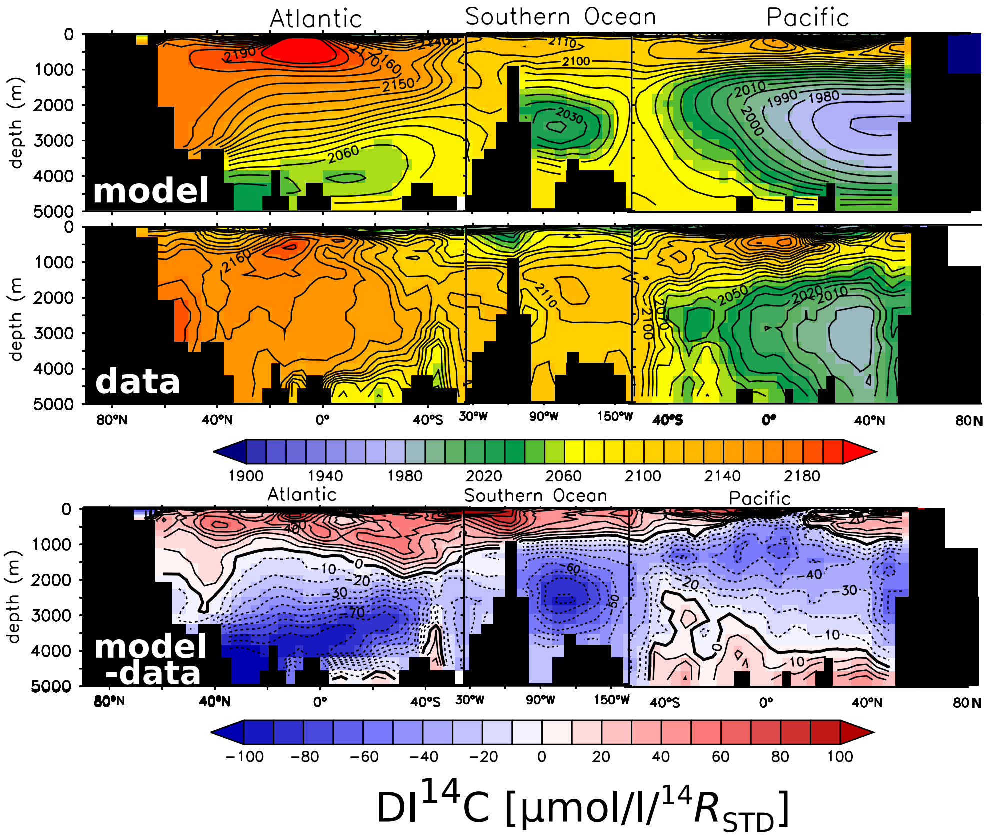

Fig. 7. Comparison of modern modelled and data-based (GLODAP,WOA09) oceanic distribution of ^{14}C in its dominant form of dissolved inorganic carbon (DI^{14}C) along a transect through the Atlantic, Southern Ocean and Pacific. The lowest panel shows the model-data difference.

CPD

9, 1165–1235, 2013

Radiocarbon production and solar activity

R. Roth and F. Joos

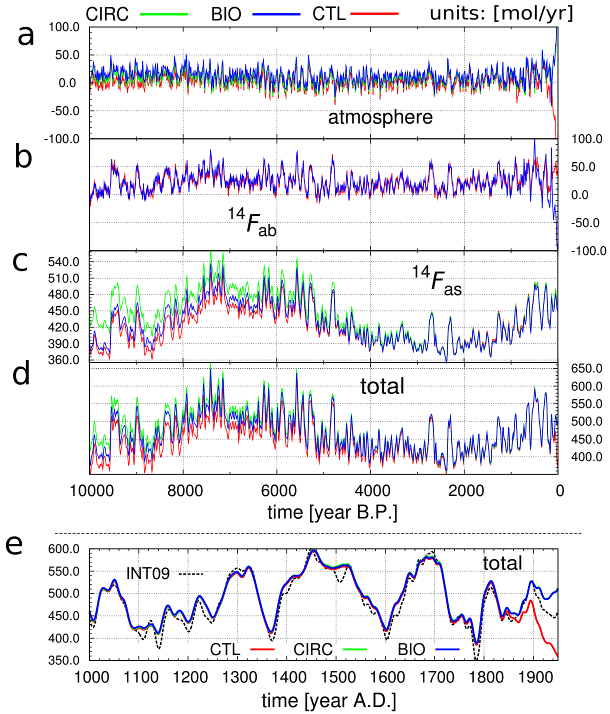

Fig. 8. Holocene ^{14}C fluxes in mol ^{14}C yr^{-1} for the different experiments: **(a)** changes and decay of the atmospheric inventory (including F_{budget}), **(b)** air-biosphere flux (F_{ab}), **(c)** air-sea flux (F_{as}) and **(d)** the sum of these contributions yielding the total production rate Q. Panel **(e)** shows the last 1000 yr in greater detail together with an experiment (INT09) where the entire globe is forced with the Northern Hemisphere dataset IntCal09 (dashed line), thereby neglecting the interhemispheric gradient in Δ^{14}C. Note that the timeseries shown in **(a)** and **(b)** have been smoothed with a cutoff of 40 yr (only for the visualization) while panels **(c)**–**(e)** show 20 yr smoothed data as described in the main text.

CPD
9, 1165–1235, 2013

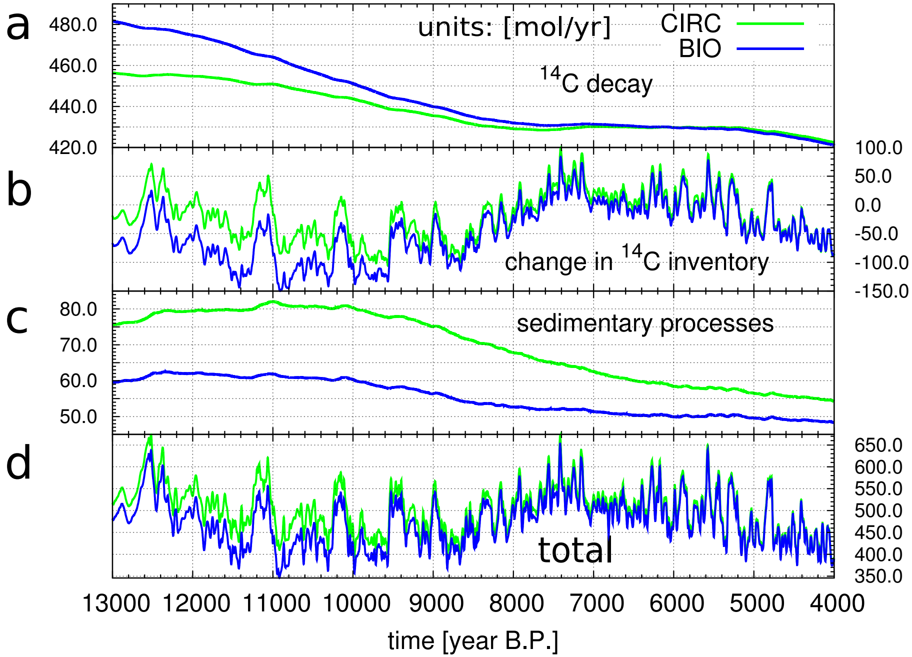

Fig. 9. The oceanic ^{14}C budget for the experiments BIO and CIRC for the last part of the glacial termination I and the early Holocene. **(a)** Decay of the data-normalized inventory of ^{14}C in the form of inorganic and organic carbon, **(b)** changes in whole ocean radiocarbon inventory, **(c)** contribution from sediments (burial flux and decay of ^{14}C within the active sediment layer). After 4 kyr BP, the two experiments do not show significant differences in the total ocean-sediment ^{14}C loss **(d)**.

CPD
9, 1165–1235, 2013

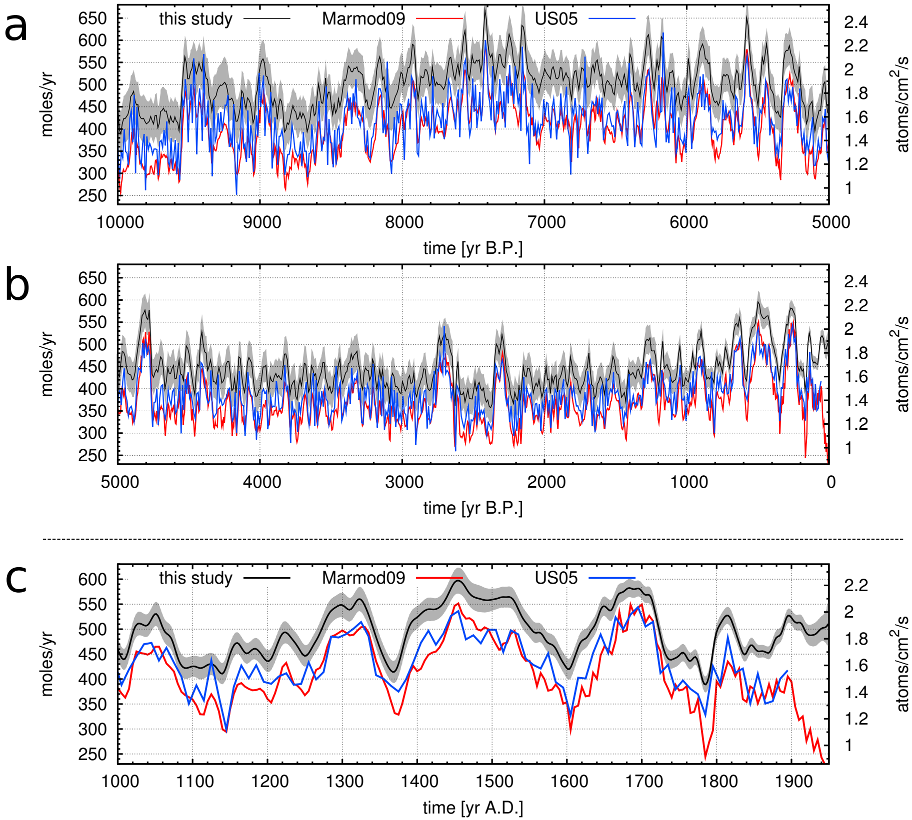

Fig. 10. (a, b) Total ^{14}C production rate from this study (black line with gray 1σ shading) and the reconstructions from Usoskin and Kromer (2005) (violet) and the output of the Marmod09 box-model (red). The gray shading indicates $\pm 1\sigma$ uncertainty as computed from statistical uncertainties in the atmospheric $\Delta^{14}C$ records, in the processes governing the deglacial CO_2 increase, air–sea gas transfer rate and global primary production on land (see Appendix and Fig. A1). **(c)** Shows the last 1000 yr of the production record in more detail.

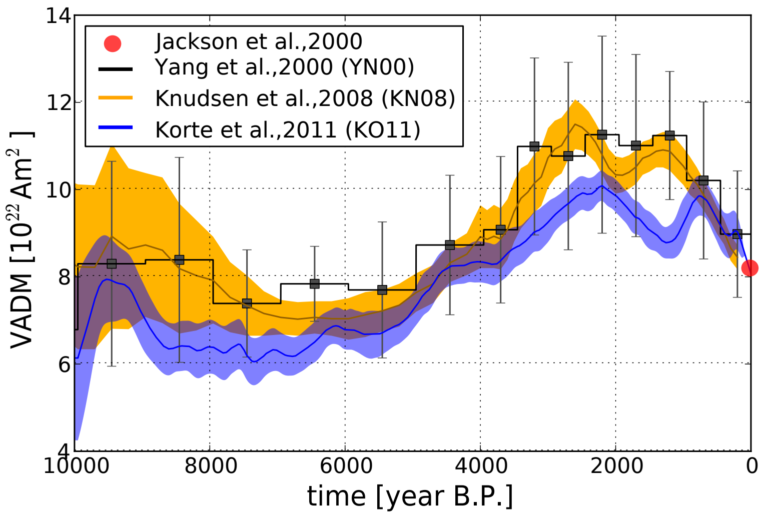

Fig. 11. Reconstructions of the virtual axis dipole moment (VADM) of the geomagnetic field for the Holocene. Black: Yang et al. (2000), orange: Knudsen et al. (2008), blue: Korte et al. (2011). For the most recent epoch the estimate of Jackson et al. (2000) yields 8.22×10^{22} Am^2 (red dot). In the present study, the data of Korte et al. (2011) is used.

CPD
9, 1165–1235, 2013

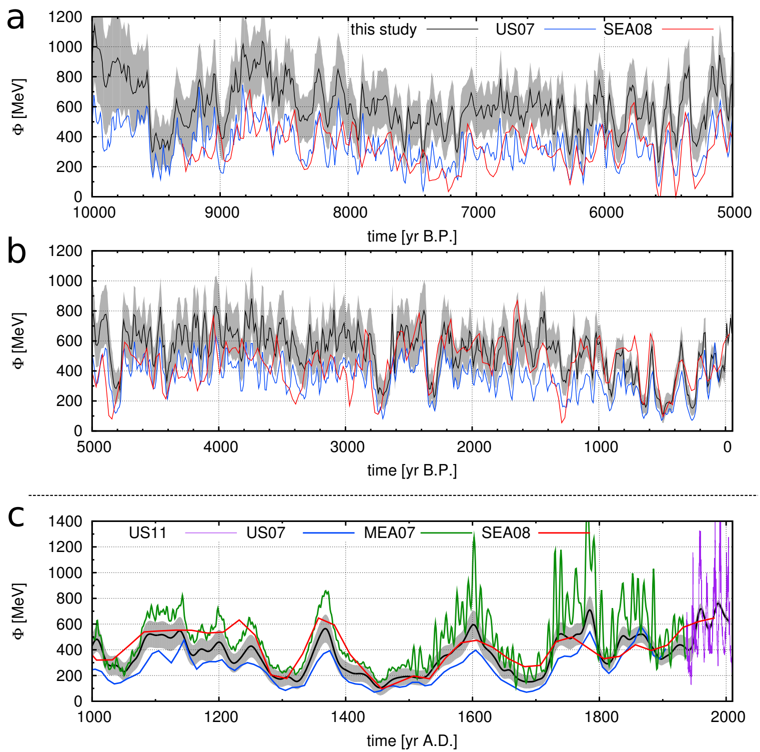

Fig. 12. (a, b) Solar modulation potential Φ based on the reconstructed radiocarbon production and the VADM history of Korte et al. (2011). The Φ-histories of Usoskin et al. (2007) (US07, blue) and of Steinhilber et al. (2008) (SEA08, red) are shown additionally. For the last millennium **(c)**, we include the Φ record from Muscheler et al. (2007) (MEA07, green) as well as the instrumental data compiled by Usoskin et al. (2011) (US11, violet). The latter was used for normalization and extension of our Φ reconstruction over recent decades. Note that all Φ's are normalized to the LIS of Castagnoli and Lal (1980) for according to Herbst et al. (2010).

CPD
9, 1165–1235, 2013

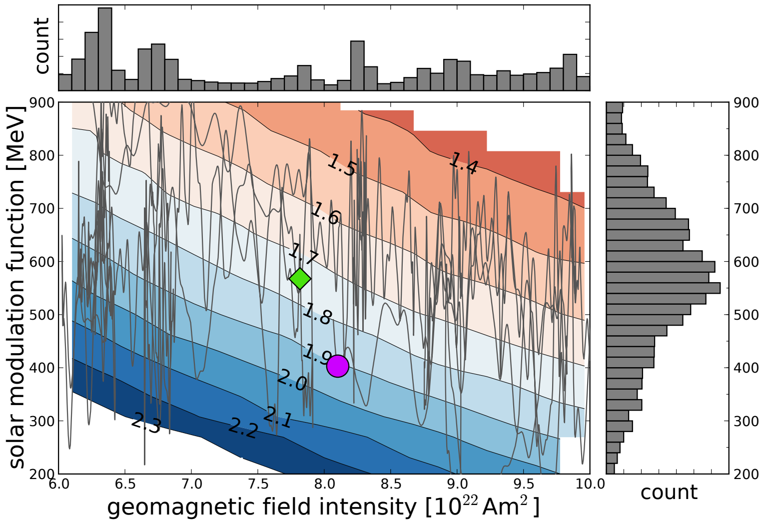

Fig. 13. The absolute radiocarbon production rate plotted as a function of the solar modulation parameter Φ and VADM. Yearly values of the smoothed Q record are used (with a cutoff period of 20 yr as in Fig. 10). The path taken by the model in this (Φ,VADM)-space is indicated by the thin gray line. The circle shows the value of Φ for the normalization period 1937–1950 as reported by Usoskin et al. (2011). The diamond shows the average production rate over the entire Holocene. On the sides of the figure, two histograms are displayed showing the relative occurrence of certain VADM (top panel) and Φ (right panel) values, ∼ 570 MeV being the most frequent modulation potential during the Holocene.

CPD
9, 1165–1235, 2013

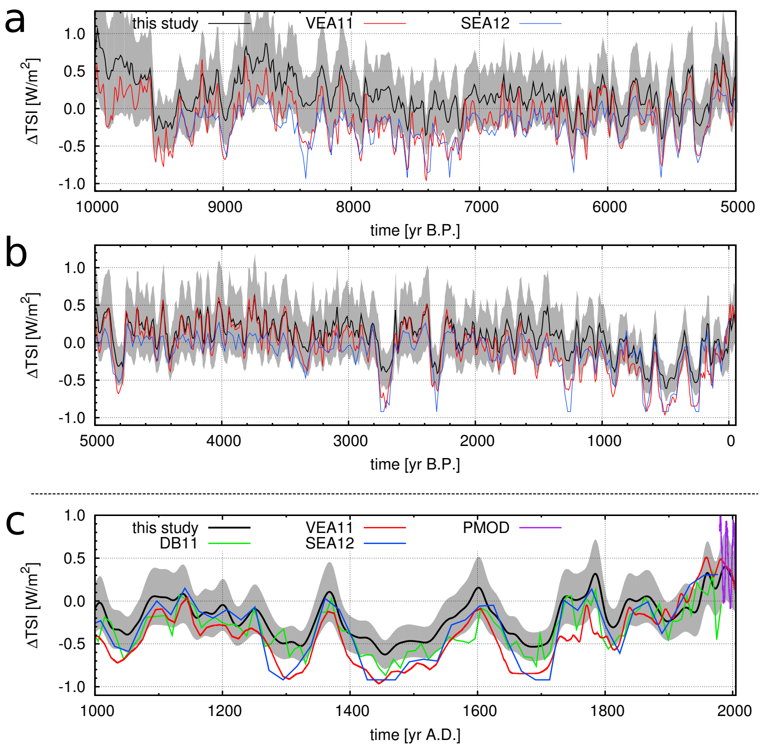

Fig. 14. (a, b) Total solar irradiance deviation from solar cycle minimum value in 1986 (assumed to 1365.57 $W m^{-2}$) calculated in this study (black with gray 1 σ error), the reconstruction by Vieira et al. (2011) (VEA11, red) and Steinhilber et al. (2012) (SEA12, blue). **(c)** Magnification of the last 1000 yr, in addition to VEA11 and SEA12 the data of Delaygue and Bard (2011) (DB11, green) is shown as well as the PMOD composite record.

CPD
9, 1165–1235, 2013

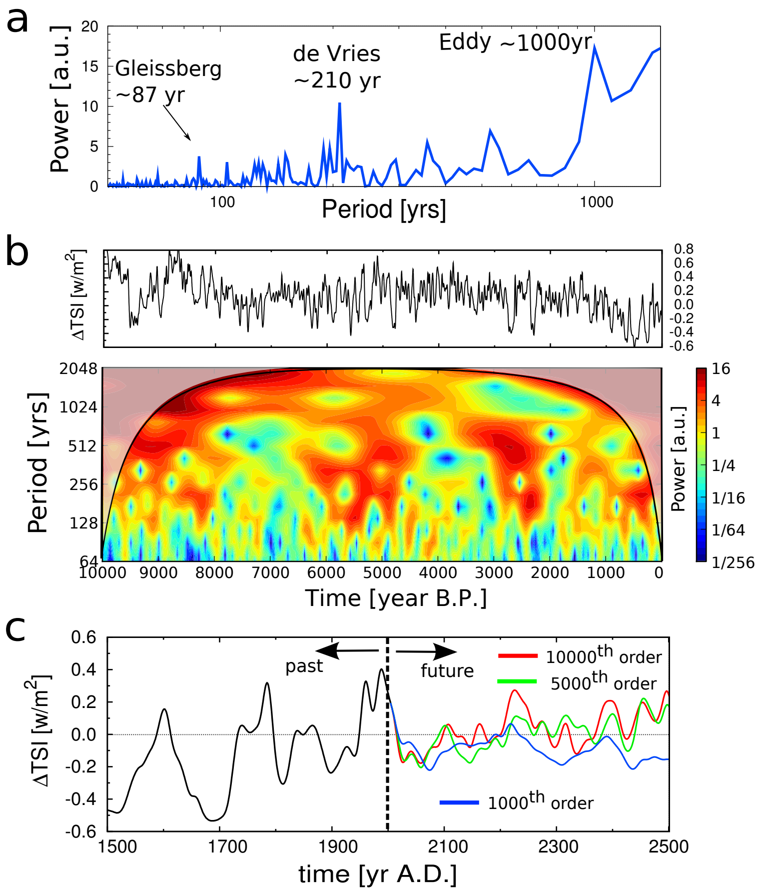

Fig. 15. **(a)** Power spectrum our TSI record up to periodicities of 2000 yr. The most dominant periodicities correspond to the Gleissberg, de Vries and Eddy cycles. **(b)** Wavlet power spectrum calculated with a Morlet-wavelet with $\log_2$ periodicity axis and color shading. **(c)** Extrapolation of the solar irradiance using an auto-regressive (AR) model (Burg method) with different orders.

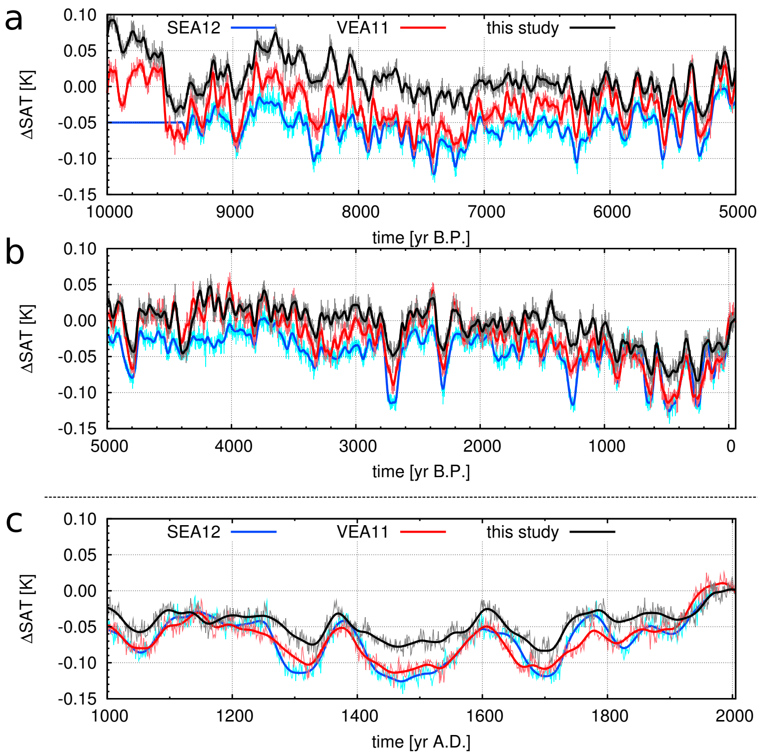

Fig. 16. (a, b) Simulated changes in SAT as a response to different TSI forcings: this study (black), VEA11 (red) and SEA12 (blue). The anomalies were calculated as the difference between two transient simulations, one with all forcings and the other with the same forcings but solar forcing taken to be constant. The last 1000 yr are shown again in panel **(c)**. In all panels, thin lines show annual data while thick lines show smoothing splines with a cutoff period of 50 yr.

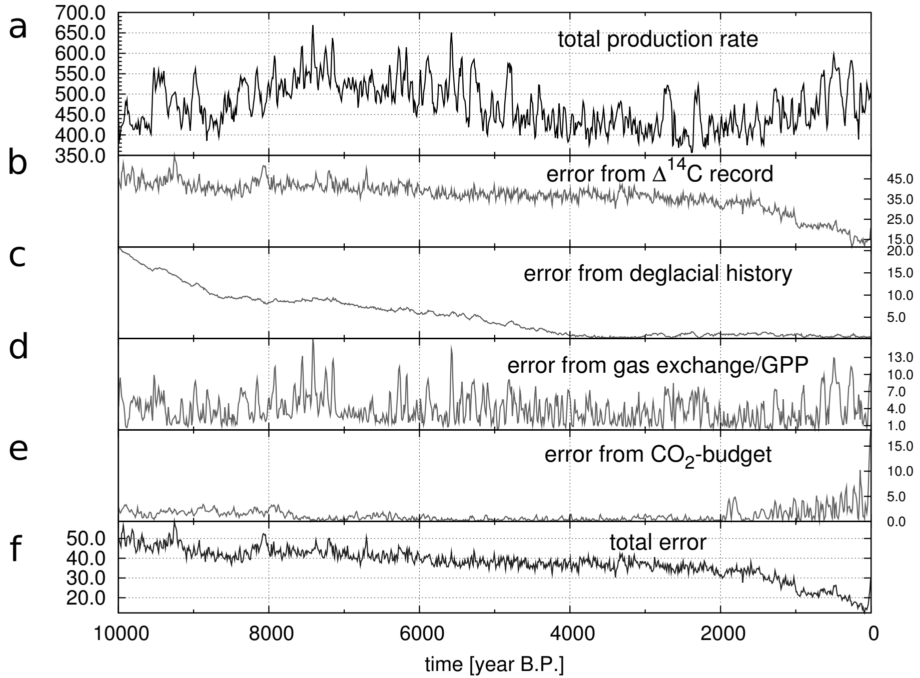

Fig. A1. Assessment of uncertainties in our production rate record. **(a)** Radiocarbon production rate (arithmetic mean of CIRC and BIO), **(b)** the uncertainty stemming from the pre-Holocene carbon-cycle evolution calculated as the absolute difference between results from simulations BIO and CIRC, **(c)** the smoothed 1σ error from the $\Delta^{14}C$ record (as shown in Fig. 2b) is calculated by a Monte-Carlo approach including 100 individual simulations and **(d)** the uncertainty in air–sea and air–land fluxes deduced by sensitivity experiments. The total error in production **(e)** varies between 50 and 10 mol yr^{-1}, corresponding to a relative error of ~10 to 2.5 %. The bulk uncertainty in the average level of Q resulting form an uncertain ocean (and land) inventory is not included in this calculation. We estimate this uncertainty to be ~15 %.

CPD
9, 1165–1235, 2013

Radiocarbon production and solar activity

R. Roth and F. Joos

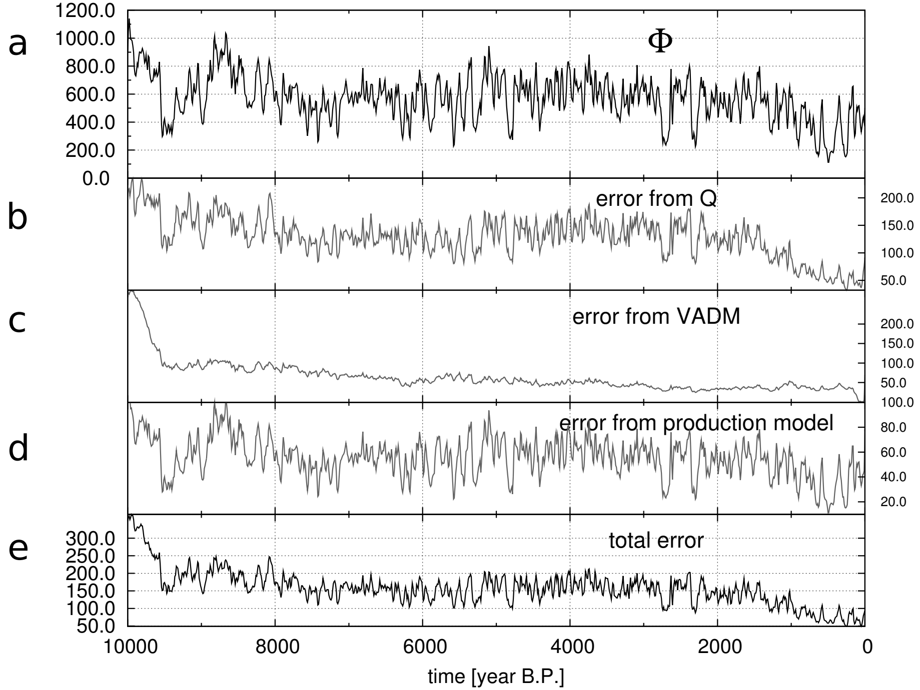

Fig. A2. Assessment of uncertainties in the solar modulation potentialΦ. **(a)** Best estimate of Φ (mean of the Monte-Carlo simulations), **(b)** uncertainty in Φ from uncertainties in the radiocarbon production Q, **(c)** from the uncertainty in the VADM reconstruction by Korte et al. (2011), **(d)** the uncertainty in the model to convert production into Φ, and **(e)** total 1σ uncertainty in the MC calculation.

CPD
9, 1165–1235, 2013

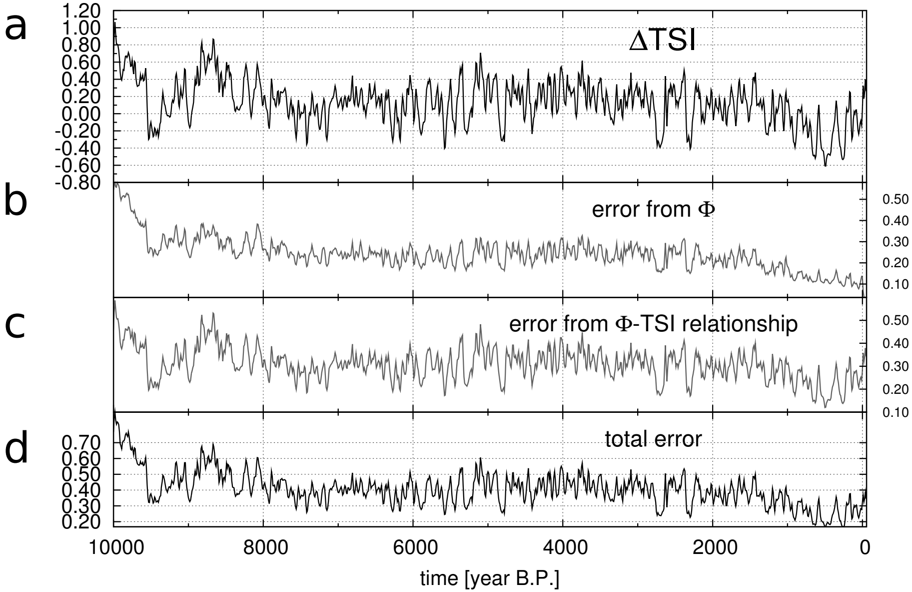

Fig. A3. Assessment of uncertainties in the ΔTSI reconstruction in $W\,m^{-2}$. **(a)** ΔTSI (mean of the Monte-Carlo simulations), **(b)** the uncertainty in ΔTSI from the error of Φ, **(c)** from the uncertainty in the TSI-B_r relationship, and **(d)** when considering all uncertainties in the MC calculation. Errors are 1σ uncertainties.

CPD
9, 1165–1235, 2013